Modeling the Formation of Eddy Dipoles at Cape St. James

by

Wendy Callendar
B. Sc., University of Victoria, 2005

A Thesis Submitted in Partial Fulfillment
of the Requirements for the Degree of

MASTER OF SCIENCE

in the School of Earth and Ocean Sciences

Supervisory Committee

Modeling the Formation of Eddy Dipoles at Cape St. James

by

Wendy Callendar
B. Sc., University of Victoria, 2005

Supervisory Committee
Dr. Jody Klymak, (School of Earth and Ocean Sciences)
Supervisor

Dr. Mike Foreman (Institute of Ocean Sciences, DFO)
Co-Supervisor or Departmental Member

Dr. Eric Kunze (School of Earth and Ocean Sciences)
Departmental Member

Dr. Chris Garrett (School of Earth and Ocean Sciences)
Additional Member

Abstract

We present here a theory for the generation of mesoscale eddies, in the context of describing the generation of dipoles seen near the Queen Charlotte Islands in British Columbia. The Regional Ocean Modeling System (ROMS) is used to show dipoles forming from the coalescence of small headland eddies at Cape St. James. These headland eddies are formed by frictional generation of potential vorticity (PV) when the tide oscillates across the cape. Only 20% of the PV generated at the cape ends up in the headland eddies, with the remainder lost due to mixing of waters with PV of opposite signs. Coalescence of the headland eddies is achieved with a much higher efficiency – the PV contained in the final eddy is near 80% of the sum of that contained in the small eddies. Not all headland eddies coalesce. Coalescence of a positive PV eddy occurs only when the eddy is formed on a strong tidal flood followed by a weak ebb. Thus, a diurnal inequality in the tides is a requirement for coalescence. The eddies in the final dipole contain roughly equal amounts of PV; each has a radius of approximately 15 km and extends to nearly 100-m depth.

Supervisory Committee
Dr. Jody Klymak (School of Earth and Ocean Sciences)
Supervisor

Dr. Mike Foreman (Institute of Ocean Sciences, DFO)
Co-Supervisor or Departmental Member

Dr. Eric Kunze (School of Earth and Ocean Sciences)
Departmental Member

Dr. Chris Garrett (School of Earth and Ocean Sciences)
Additional Member

Table of Contents

List of Tables

List of Figures

Acknowledgments

I would like to thank my supervisors Dr. Jody Klymak and Dr. Mike Foreman for their assistance and encouragement. Particularly, I am grateful for Jody's aid in giving direction to my research and Mike for modeling advice. I also thank the other members of my committee, Dr Chris Garrett and Dr. Eric Kunze who provided valuable feedback on my work.

The potential vorticity budget used herein would not have been possible without the initial Matlab code and assistance provided by Dr. Leif Thomas. Dr. Manu Di Lorenzo also provided help with model set up for the Queen Charlotte Islands region.

This work was funded primarily through a grant from BC Energy, Mines and Petroleum Resources, for which I am grateful.

I am very thankful to the other graduate students that I worked with in the past few years. My office mates helped me to maintain my sanity during difficult times so I thank Reyna Jenkins, Shani Rousseau, Jeannette Bedard and Mei Sato. Also, Laura Bianucci was extremely helpful in answering so many of my modeling questions and giving me someone with whom I could complain about ROMS.

Lastly, I thank my family and particularly my wonderful husband Chris for their support and encouragement.

1. Introduction

Eddies are an important mechanism for transporting nutrients and other tracers long distances. For example, a single Haida eddy transports 3000 to 6000 km^3 of coastal water, carrying nutrients up to 1000 km and persisting for several years (Whitney and Robert, 2002). The westward flux of salt in meddies has been estimated at 4000 ‰ m^2/s, leading to the supposition that meddies are likely a significant part of the westward salinity flux in the Mediterranean water salt tongue (McWilliams, 1985).

Eddies may be generated in three ways: (i) through baroclinic instability, (ii) via a mixing event followed by geostrophic adjustment, or (iii) through friction and flow separation. The first of these, baroclinic instability, requires strong geostrophic currents, such as the Gulf Stream (Gill, 1982). While the formation of Sitka eddies at the Alaskan Panhandle has been attributed to baroclinic instability (Melson et al., 1999; Thomson and Gower, 1998), the current responsible for this instability is wind-driven. Since we do not include wind-forcing in our model, and there are no other strong, perpetual currents in this region, eddy generation via baroclinic instability is not relevant to this study.

The second generation mechanism, geostrophic adjustment of mixed water, was hypothesized by McWilliams (1985) to be the cause of SCV (submesoscale coherent vortex) formation. SCV's are vortices with horizontal scales not greater than the first baroclinic radius of deformation; they are found throughout the world's oceans and have a predominantly anticyclonic rotation. This last characteristic requires them to have a generation mechanism which produces a rotational bias. Adjustment of a mixed patch will generate an anticyclonic vortex since a mixed patch is less stratified than the surrounding waters and so will develop a balancing anticyclonic circulation.

D'Asaro (1988) explored the final method, friction and flow separation, while investigating submesoscale eddies in the Beaufort Sea. While these eddies fit the description for SCV's, he argued that they could not have been generated through

mixing. For a homogeneous system, as would be produced by a mixing event, the appropriate expression for potential vorticity (PV) is (Gill, 1982):

$$q = \frac{\zeta + f\hat{k}}{H}$$

where q is the PV, ζ and f the relative and absolute vorticity respectively and H the depth of the mixed region. In the case of these particular eddies, the depth of the mixed region required to produce the observed change in ζ was unreasonably large, exceeding the total depth of the generation region. D'Asaro proposed instead that the vorticity was produced via bottom friction. Flow passes through a canyon, intensified on the right-hand side of the canyon by the Coriolis force (see Figure 1.1 for a cartoon of this process). The velocity maximum is near the right-hand side, decaying to zero at the wall in a frictional boundary layer. Relative vorticity within this boundary layer is thus negative. At the end of the canyon, the coast veers sharply to the right, causing the flow to separate and the negative vorticity in the water is manifested as anticyclonic eddies.

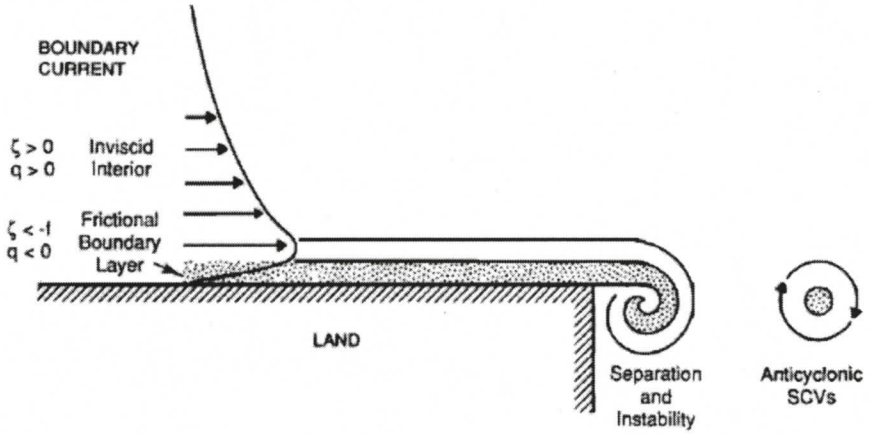

Figure 1.1 A cartoon used by D'Asaro (1988) to explain the generation of SCV's in the Beaufort Sea.

Tidal flow across a cape may generate eddies in much the same way as described by D'Asaro (Pawlack and MacCready, 2002). However, rather than generating a continuous stream of eddies rotating the same way, oscillating tides generate eddies which rotate in

alternating directions. The formation and behaviour of these eddies can be predicted based on the values of two parameters (Signell and Geyer, 1991). The first expresses the relative importance of advection and bottom friction: $\mathrm{Re}_f = H/C_d a$ where H is the water depth away from the cape, C_d is the drag coefficient and a the headland length (alongshore extent). The second parameter is the Keulegan-Carpenter number: $K_c = U_o/\sigma a$ which relates advection to local acceleration. For the case $K_c < \mathrm{Re}_f$, an eddy will be formed on each half-cycle of the tide. Friction is weak enough that an eddy lasts to interact with the eddy generated on the successive tide. The two eddies form a dipole and self-advect away from the cape.

To generate an eddy at all, there must be separation of the boundary layer from the cape (Kundu, 2004); separation will occur if the radius of curvature of the cape is less than H/C_d where H is the constant water depth away from an initial slope at the coastline and C_d a bottom friction coefficient (Garrett, 1995). So, for a depth H of 50 m and $C_d \cong 1e-3$, separation will occur if the radius of curvature for the cape is 50 km or less.

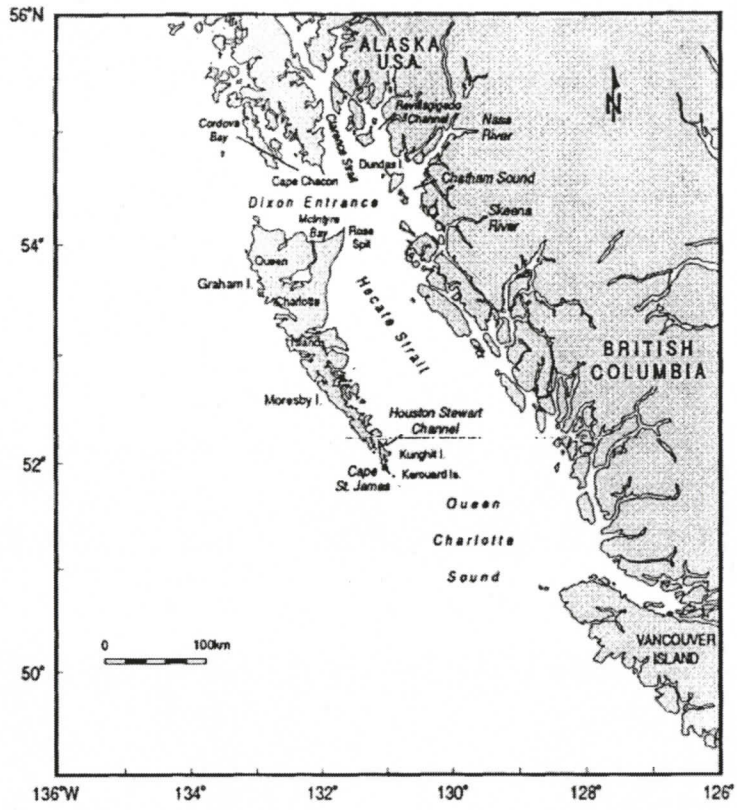

Figure 1.2 The geography of the north coast of British Columbia. Figure courtesy of Ballantyne et al., 1996.

In this study, we are interested in eddy dipoles generated at Cape St James (Figure 1.2). There have been other studies of eddy generation at this cape, most notably to look at generation of Haida eddies (see Figure 1.3), a large wintertime feature which is responsible for the transport of nutrient-rich coastal water into the Gulf of Alaska (Whitney and Robert, 2002). Crawford et al. (2002) hypothesized that these eddies were generated due to northward winter winds piling surface water in Hecate Strait. The southward return flow was concentrated to the west side of the strait due to the Coriolis force. This buoyant current would separate from the shore when it passed Cape St James to form an eddy as seen in the laboratory studies of Cenedese and Whitehead (2000). This idea was refined by Di Lorenzo et al. (2005) who reproduced Haida eddies in a ROMS model but, rather than a single separation from the cape producing a Haida eddy, it was found that a succession of smaller (~80 km diameter) eddies generated at the cape would merge together to form a large (~200 km diameter, extending to 1000 m depth)

eddy. The generation cycle lasted 3-4 months, consistent with observations (Whitney and Robert, 2002).

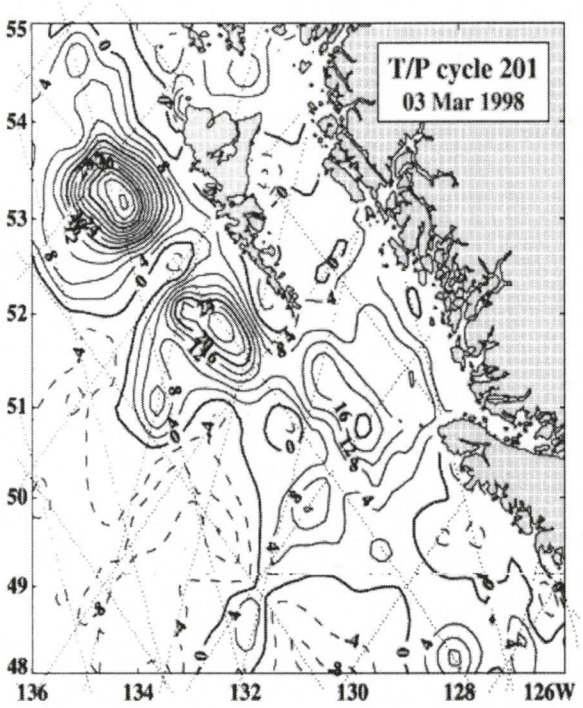

Figure 1.3 Contour plot of sea level anomalies based on altimetry data from TOPEX/Poseidon and ERS-2 satellites. Two Haida eddies which detached off of Cape St James in the Winter of 1998. These two eddies later merged to form one very large eddy. Figure courtesy of Crawford et al., 2002.

Another study of eddy generation at Cape St. James was done by Thomson and Wilson (1987) who looked at tidal rectification as a way of explaining a pair of eddies seen in density and sea surface height fields (Figure 1.4). One eddy was anticyclonic and seen directly west of Cape St James; the second eddy was cyclonic, weaker than the first, and could be found south of the cape. Both eddies had radii near 20 km. Model results with an idealized cape and flat bathymetry implicated tidal rectification as the generation mechanism because current variability in the eddies at fortnightly and monthly periods was quite marked.

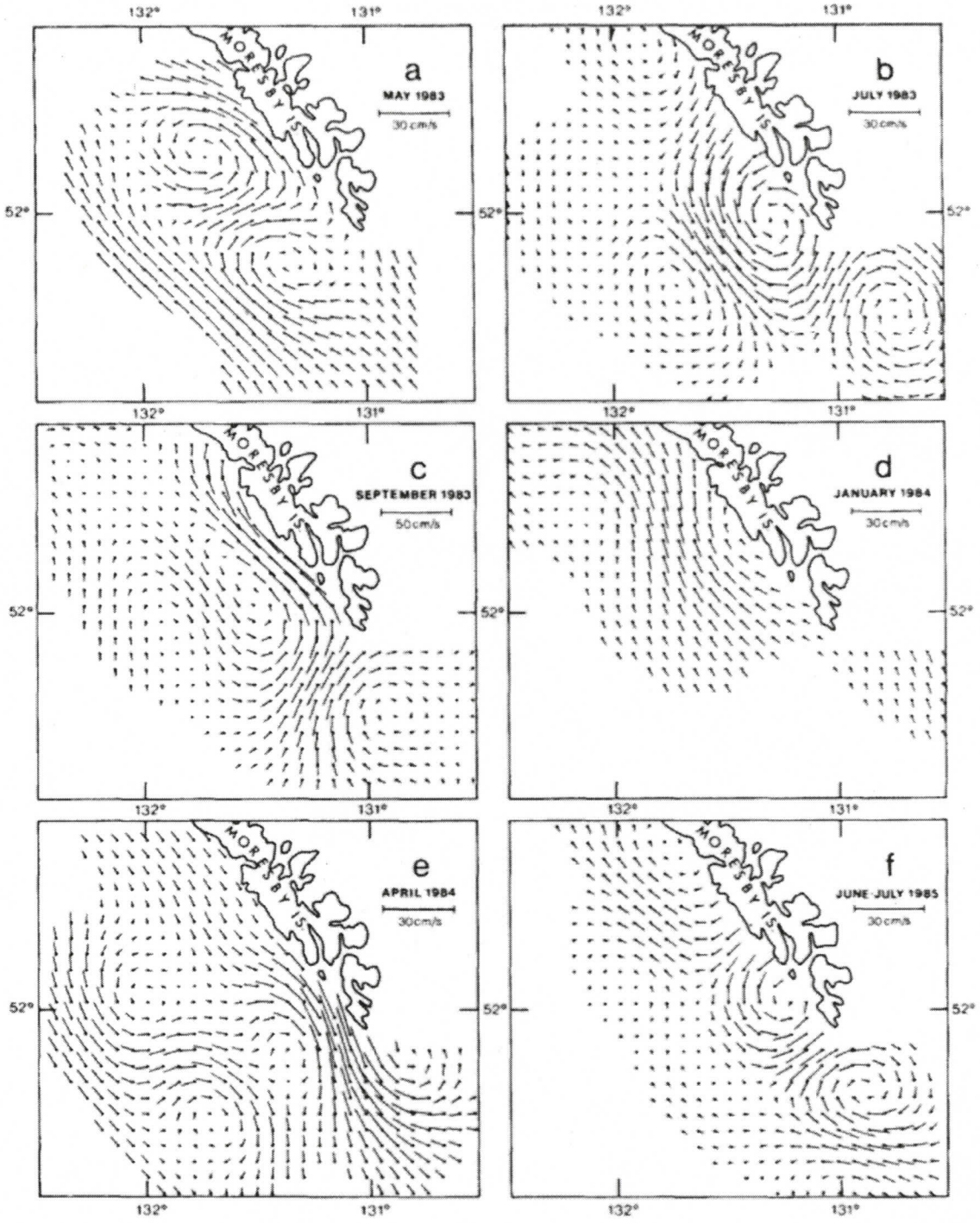

Figure 1.4 Geostrophic surface currents derived from objectively mapped dynamic height contours. Currents are directed away from the dots. Note speed scale change in (c). This is Figure 10 from Thomson and Wilson (1987).

The features of interest here are dipoles formed at Cape St James, likely the same as those investigated by Thomson and Wilson (1987). Some examples seen in satellite fluorescence images can be seen in Figure 1.5. It should be noted that these images are not from randomly chosen dates, but were specifically chosen because they were evocative of the feature in the model. Each eddy in the dipoles highlighted in these images has a diameter ranging from 20 to 40 km and appears to be generated at Cape St James. While we do not have images specifically showing these eddies having moved great distances from the cape, a study of these dipoles is warranted given the propensity of many other eddies to transport their core water-mass long distances. This document is arranged as follows: chapter 2 discusses the setup of the model used and describes a numerical tool used to identify the generation mechanism of the headland eddies; chapter 3 presents the model results for the generation of these eddies in a purely qualitative way; chapter 4 quantifies the mechanism seen in chapter 3 and presents an estimate for its efficiency; chapter 5 is a summary and discussion.

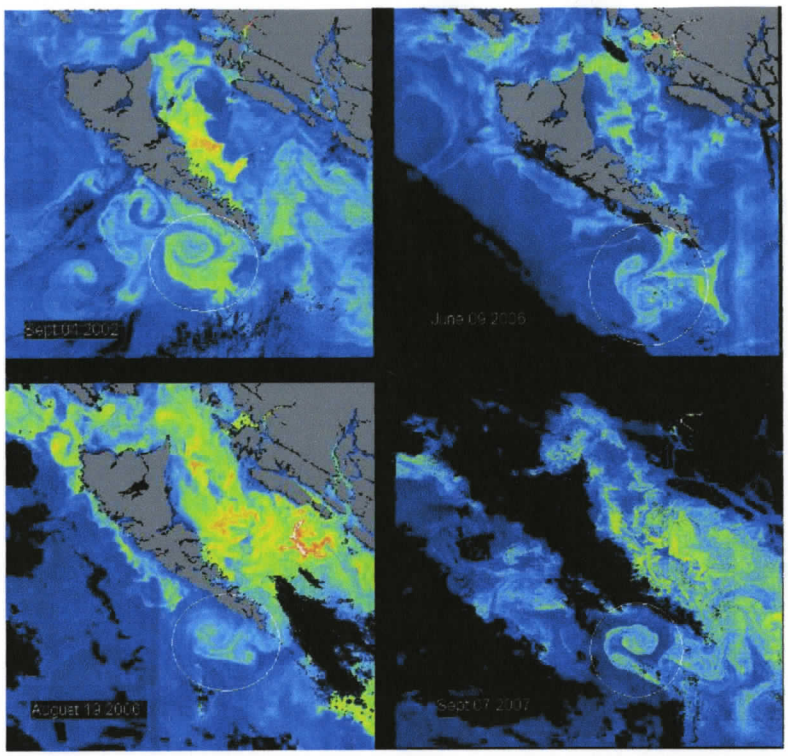

Figure 1.5 MERIS satellite fluorescence images of eddy dipoles near Cape St James. Data provided by the European Space Agency. Image provided by Stephanie King and Jim Gower at the Institute of Ocean Sciences (IOS), Fisheries and Oceans Canada. Image funding by the Canadian Space Agency

2. Methods

2.1 Model setup

The model used was the Regional Ocean Modeling System (ROMS) version 3.0 which has garnered much usage in recent years (Capet et. al., 2008; Choi and Wilkin, 2007; Warner et al., 2005a), including studies of mesoscale eddy generation (Foreman et al., 2008, Di Lorenzo et al., 2005, Serra et al., 2005). The grid domain is shown in Figure 2.1. The axes are rotated by 39 degrees such that the x and y axes run cross-shelf and along-shelf respectively, similar to models for this region used by Cummins and Oey, 1997 (hereafter referred to as CO97) and Di Lorenzo et al., 2005 (DFC05). The horizontal resolution varies in the x-direction from 1.25 km along the southeastern boundary to 750 m over the shelf break to a constant 1 km inside the shelf break. Resolution in the y direction is a constant 1 km.

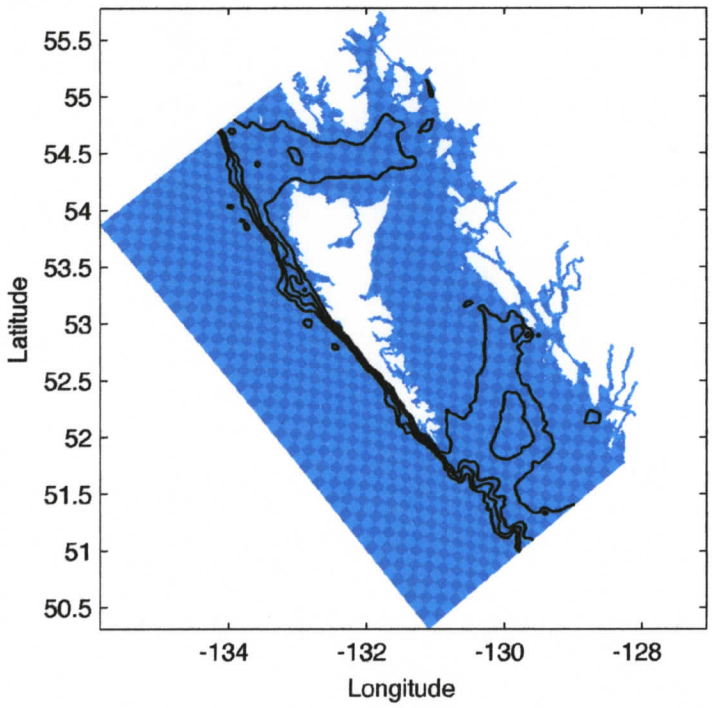

Figure 2.1 Model grid used; each square represents a 10 by 10 set of grid cells. Contours are shown at 200, 500, 800 and 1100 m depth.

ROMS is a terrain-following model, meaning that there is the same number of vertical levels everywhere, called σ levels. We use 20 σ levels here (similar to CO97 and DFC05), with increased resolution near the surface and bottom boundary layers. σ is an evenly spaced vector between -1 and 0, where the number of elements equals the number of vertical layers in the model. ROMS defines the depth of each sigma layer by the equation (Song and Haidvogel, 1994):

$$z = \zeta + \left(1 + \frac{\zeta}{h}\right)\left[h_c\sigma + (h - h_c)C(\sigma)\right] \tag{2.1}$$

where ζ is the sea surface height, h the water depth, h_c a critical depth above which there is enhanced vertical resolution and $C(\sigma)$ defines how the resolution is distributed:

$$C(\sigma) = (1-b)\frac{\sinh(\theta\sigma)}{\sinh(\theta)} + b\frac{\tanh\left[\theta\left(\sigma + \frac{1}{2}\right)\right] - \tanh\left(\frac{1}{2}\theta\right)}{2\tanh\left(\frac{1}{2}\theta\right)} \tag{2.2}$$

where θ controls how much extra resolution goes into the surface and bottom boundary layers and b controls how much of that extra resolution is concentrated near the bottom. For this simulation, the values used were θ=3 and b=0.4, values recommended by the ROMS community (Arango, 2004).

The horizontal resolution used here is finer than that used in previous studies of this area (CO97 and DFC05 each had horizontal resolutions of 5 km) in an effort to maintain the steep bathymetry characteristic of the continental shelf in this region, while keeping spurious flows to a reasonable level. These flows appear due to errors in the pressure calculation of all sigma coordinate models, as was first described by Haney (1991). The method ROMS uses for calculating the pressure gradient force is described in Shchepetkin and McWilliams (2003). To summarize the problem, a vertical

extrapolation of density is required to obtain a horizontal pressure gradient when adjacent grid points are at excessively different depths. A metric defined for this problem is

$$r_x = \frac{(z_4 + z_3) - (z_2 + z_1)}{(z_4 - z_3) + (z_2 - z_1)} \tag{2.3}$$

where z_1, z_2, z_3 and z_4 are the depths at the corners of a single (vertical) grid cell; bottom left, top left, bottom right, and top right respectively. When $r_x > 1$, extrapolation (rather than interpolation) is required to calculate density. The ROMS community suggests that r_x should maximally be about 5 or 6 (Shchepetkin, 2007) for a realistic application. Providing only minimal smoothing of bathymetry data, the distribution of resolution described above obeys $r_x < 6.5$ over the whole grid, and $r_x < 5.5$ in the region of interest. The original bathymetry data was extracted from the ETOPO6 database, and a minimum depth was set to 10 m in order to avoid the creation of mud flats at low tide.

The model boundaries were far enough away from the region of interest that 3-D momentum and tracer boundary conditions clamped to initial conditions were satisfactory; Flather and Chapman conditions governed the 2-D momentum and free-surface boundaries, respectively. More information on the model numerics may be found in Shchepetkin and McWilliams (2003, 2005).

Initial conditions consisted of zero motion and a horizontally uniform stratification representative of the summer stratification for this region (based on the stratification used by CO97); it is defined by a linear trend in salinity and temperature near the surface, followed by an exponential drop off at depth (fig 2.2).

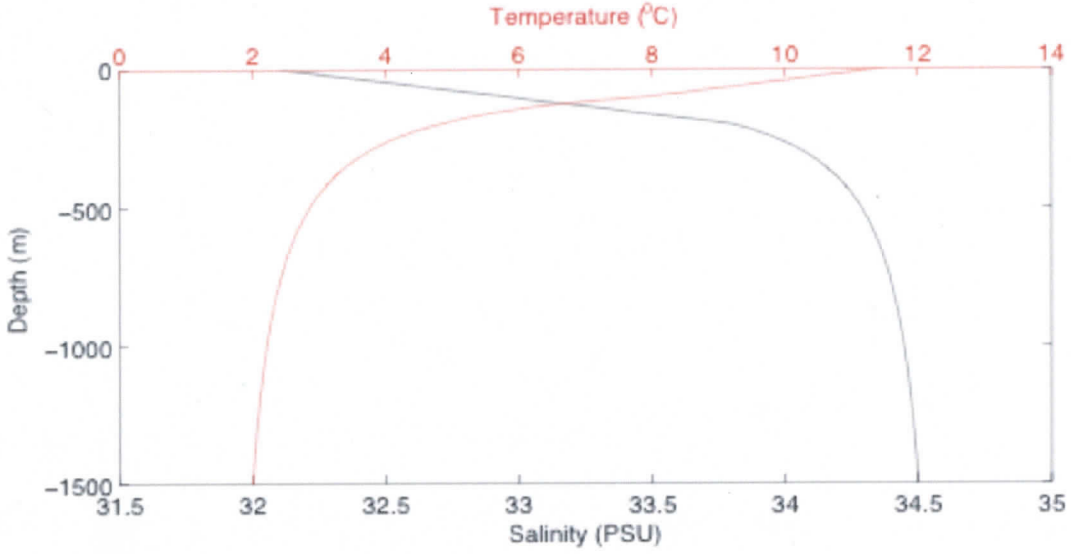

Figure 2.2 Initial temperature and salinity profiles used in the base model run

Data for tidal forcing at the model boundaries was interpolated from the Foreman et al. (2000) northeast Pacific Ocean model that assimilated tidal harmonics computed from TOPEX/Poseidon altimetry (Cherniawsky et al. 2001). Only the K1, O1, M2, and S2 constituents were used as in CO97 instead of the eight constituents used by Foreman et al. (1993) and Ballantyne et al. (1996). The barotropic response in CO97 agreed well with the eight constituent models, demonstrating the four constituents unused by CO97 account for a very small percentage of the total tidal variance in the region.

Turbulence closure is achieved via a k-theory parameterization (Holton, 2004), where the eddy covariance terms in the eddy-averaged momentum and thermodynamic equations are estimated using gradients in the average velocity and density fields:

$$\overline{u_i u_j} = K_M \frac{\partial U_i}{\partial x_j}; \qquad \overline{\mathbf{u}'\rho'} = K_H \nabla \rho. \tag{2.4}$$

Here K_M is the eddy viscosity and K_H the eddy diffusivity; each of these values is defined differently for the horizontal and vertical directions.

The parameterization used for the vertical components of these equations was the k-epsilon closure (Warner et al., 2005). With this closure, $K_M = \sqrt{2kl}S_M + \upsilon$ where $\upsilon = 1e-5\ m^2/s$ is the molecular viscosity, or background K_M value and $K_H = \sqrt{2kl}S_H + \upsilon_\vartheta$ where $\upsilon_\vartheta = 1e-6\ m^2/s$ is the molecular diffusivity, or background K_H value. $S_M = 0.4$ and S_H (see Warner et al., 2005 for the full definition) are stability functions calculated according to Kantha and Clayson (1994). k is the turbulent kinetic energy and l the turbulent lengthscale.

k-epsilon is a two equation closure, the two equations being for k and ε, which is turbulent dissipation of k:

$$\begin{aligned}
&\frac{\partial k}{\partial t} + \mathbf{u}\cdot\nabla k = \frac{\partial}{\partial z}\left(\frac{K_M}{\sigma_k}\frac{\partial k}{\partial z}\right) + P + B - \varepsilon \\
&\frac{\partial \varepsilon}{\partial t} + \mathbf{u}\cdot\nabla \varepsilon = \frac{\partial}{\partial z}\left(\frac{K_M}{\sigma_\varepsilon}\frac{\partial \varepsilon}{\partial z}\right) + \frac{\varepsilon}{k}\left(c_{\varepsilon 1}P + c_{\varepsilon 3}B - c_{\varepsilon 2}\varepsilon\right) \\
&P = -\langle u'w'\rangle\frac{\partial u}{\partial z} - \langle v'w'\rangle\frac{\partial v}{\partial z} = K_M M^2, \qquad M^2 = \left(\frac{\partial u}{\partial z}\right)^2 + \left(\frac{\partial v}{\partial z}\right)^2 \\
&B = -\frac{g}{\rho_0}\langle \rho'w'\rangle = K_H N^2, \qquad\qquad N^2 = -\frac{g}{\rho_0}\frac{\partial \rho}{\partial z}.
\end{aligned} \tag{2.5}$$

$\sigma_k = 1.0$ is the turbulent Schmidt number for k. P and B are turbulent production by shear and buoyancy. $\sigma_\varepsilon = 1.3$ is the Schmidt number for the eddy diffusivity of dissipation, $c_{\varepsilon 1} = 1.44$ and $c_{\varepsilon 2} = 1.92$. $c_{\varepsilon 3} = 1.0$ in unstable stratification and $c_{\varepsilon 3} = -0.52$ in stable stratification; these values were selected (by Warner et al., 2005) to be consistent with decaying homogeneous isotropic turbulence.

The turbulent lengthscale, l, is calculated using:

$$l = \left(c_\mu^0\right)^3 k^{3/2}\varepsilon^{-1} \tag{2.6}$$

where $c_\mu^0 = -0.52$ is a stability coefficient based on experimental data for unstratified channel flow with a log-layer solution. Sample values of K_M for a profile near Cape St James over 24 hours are shown in Figure 2.3.

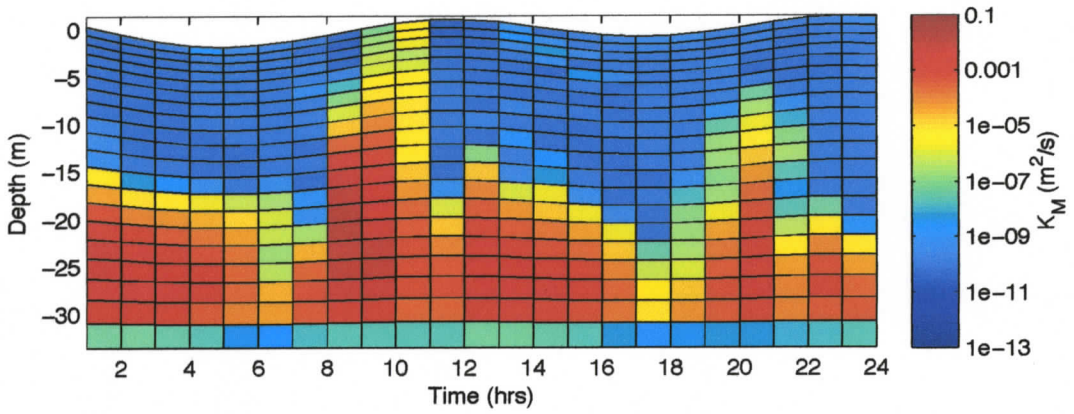

Figure 2.3 A time series of vertical eddy viscosity profiles 2 km south of Cape St James over 24 hours on day 18 of the model run. These values are taken from the maximum positive PV generation region which will be discussed in chapter 4. Maximum K_M values occur at hours 9 and 20, coinciding with the maximum current velocities on ebb tide. The disparity between current velocities on flood and ebb tides can be seen in Figure 3.5.

For more information on the k-epsilon closure and other closures available in ROMS, see Warner et al. (2005).

The value of K_M for the horizontal terms in equation 2.4 was set at a constant 5.0 m^2/s. K_H for the horizontal terms was set to zero, since the tracer advection scheme includes some inherent smoothing. We can test whether the value set for K_M affects the generation process of the features of interest by finding what horizontal scale it will smooth over in a single tidal period: if we multiply K_M by a tidal period (12.4 hours) and take its square root, we get a lengthscale of about 500 m, meaning this viscosity will smooth the momentum field over ~500 m in 12.4 hours. The features of interest in this study have a horizontal lengthscale of at least 5 km, so the value for K_M does not greatly affect their generation process.

Bottom stress was calculated using a logarithmic formulation via bottom roughness as recommended for use with the GLS closure (Warner et al., 2005). This formulation assumes a no-slip bottom boundary with a logarithmic decrease of velocities toward the boundary. The bottom stress calculation is

$$str_{\log} = k^2 \left(\log\left(\frac{zr(1) - H}{Zob} \right) \right)^{-2} u\sqrt{u^2 + v^2} \tag{2.7}$$

where $k = 0.41$ is the von Karman constant (Holton, 2004), *zr(1)* the depth of the bottom-most σ level, H the water depth, *Zob* the bottom roughness and u and v the velocities in the bottom-most sigma level in the x and y directions respectively. Formulating bottom stress in this manner means that, in deep regions, where the deepest sigma level may be many 10's of metres off the ocean bottom, a lesser stress will be experienced than in regions where the deepest sigma level is only a few metres off the bottom. This is instead of a more common linear or quadratic bottom-stress whose value is a simple function of the velocity in the bottom-most sigma level, regardless of how far off the ocean bottom this sigma level is. Here, *Zob=0.02* has been used for the bottom roughness. This may be compared to a quadratic drag coefficient by noting that bottom stress in a quadratic formulation is

$$str_{quad} = C_D u\sqrt{u^2 + v^2} \tag{2.8}$$

where C_D is the quadratic drag coefficient. We can write the logarithmic bottom stress in terms of an effective drag coefficient, $C_{D\log}$

$$str_{\log} = C_{D\log} u\sqrt{u^2 + v^2} \tag{2.9}$$

where

$$C_{D\log} = vk^2\left[\log\left(\frac{zr(1)-H}{Zob}\right)\right]^{-2}. \tag{2.10}$$

For example, at a depth H of 50 m, the bottom-most sigma level *zr(1)* is 47.88 m giving a $C_{D\log}$ value of 0.008.

2.2 Potential Vorticity budget

We are interested in understanding the formation of eddies in the model. Eddies are characterized by anomalous PV, so we diagnose the change of PV in regions of the model. The chosen control volume is bounded in the horizontal by along-shore and across-shore transects and in the vertical by two isopycnals. A logical choice for this analysis is a PV budget (Thomas, 2008, T08). T08 wrote a PV budget for use with a ROMS model to investigate the generation mechanism of intrathermocline eddies at wind-forced fronts. The model this budget was based on had a flat bottom, constant horizontal resolution and a rigid lid, so this budget was adapted for use with the more realistic model used here. This budget was based on the equation for the full Ertel PV (Gill, 1982):

$$q = \omega_a \cdot \nabla b \tag{2.11}$$

where q is the PV, $\omega_a = f\hat{k} + \nabla \times \mathbf{u}$ the absolute vorticity, $b = -g\rho/\rho_0$ the buoyancy, and f the Coriolis frequency. Changes in PV arise from advection, frictional torques, and mixing as shown by each term in the following equation (Marshall and Nurser, 1992):

$$\frac{\partial q}{\partial t} = -\mathbf{u}\cdot\nabla q + \nabla \times \mathbf{F}\cdot\nabla b + \omega_a \cdot \nabla \mathcal{D}. \tag{2.12}$$

The two generation terms are:

1) $\nabla \times \mathbf{F} \cdot \nabla b$. This term introduces PV through curls of body forces acting on surfaces of constant density; since the density gradient is largely vertical, the resulting PV is oriented in the vertical. In the model, $\mathbf{F} = \nabla \cdot \left(K_M \hat{k}\, \partial \mathbf{u_h} / \partial z \right)$ where $\mathbf{u_h} = (u,v)$.

2) $\omega_a \cdot \nabla \mathcal{D}$. Here, we have generation of PV through mixing where $\mathcal{D} = \nabla \cdot (K_H \hat{k}\, \partial b / \partial z)$. From 2.4, q is a function of the buoyancy gradient, so any change in stratification (for example due to a mixing event) will generate PV.

T08 was able to approximate the terms in equation 2.12 using ROMS which correspond to terms in the momentum and tracer equations. The tracer equations are:

$$\frac{\partial S}{\partial t} = -\mathbf{u} \cdot \nabla S + \mathcal{D}_S \tag{2.13}$$

$$\frac{\partial T}{\partial t} = -\mathbf{u} \cdot \nabla T + \mathcal{D}_T . \tag{2.14}$$

The tracer equations may be combined to form a buoyancy equation based on the equation for b given above and the model's equation of state:

$$\rho = \rho_0 - \rho_0 T_{coef} (T - T_0) + \rho_0 S_{coef} (S - S_0) \tag{2.15}$$

where the temperature and salinity coefficients, T_{coef} and S_{coef}, were set to 1.7e-4 and 7.6e-4, respectively. ρ_0, T_0, and S_0 were set to 1027 kgm^{-3}, 10 psu and 35 °C respectively. The prognostic equation for buoyancy becomes

$$\frac{\partial b}{\partial t} = -\mathbf{u} \cdot \nabla b + \mathcal{D}_b = ADVb + DIAb. \tag{2.16}$$

The momentum equations are:

$$\frac{\partial u}{\partial t} = -\mathbf{u}\cdot\nabla u + fv - \frac{1}{\rho_0}\frac{\partial p}{\partial x} + X = ADVu + CORu + PRESu + FRICu \tag{2.17}$$

$$\frac{\partial v}{\partial t} = -\mathbf{u}\cdot\nabla v - fu - \frac{1}{\rho_0}\frac{\partial p}{\partial y} + Y = ADVv + CORv + PRESv + FRICv. \tag{2.18}$$

In equations 2.16-2.18, we have labelled each term for use in later equations.

ROMS does not have a vertical momentum equation since vertical flow is defined only by convergence and divergence of horizontal flow. Since we do not have terms a vertical momentum equation would provide, T08 altered the definition for q to exclude any terms including w:

$$\tilde{q} = \left(f + \frac{\partial v}{\partial x} - \frac{\partial u}{\partial y}\right)\frac{\partial b}{\partial z} + \frac{\partial u}{\partial z}\frac{\partial b}{\partial y} - \frac{\partial v}{\partial z}\frac{\partial b}{\partial x} \tag{2.19}$$

and a prognostic equation for $\tilde{q}$ was generated from the momentum and buoyancy equations above:

$$\begin{aligned}\frac{\partial \tilde{q}}{\partial t} = &\left(f + \frac{\partial v}{\partial x} - \frac{\partial u}{\partial y}\right)\frac{\partial}{\partial z}(2.16) + \frac{\partial b}{\partial z}\frac{\partial}{\partial x}(2.18) - \frac{\partial b}{\partial z}\frac{\partial}{\partial y}(2.17) \\ &+ \frac{\partial b}{\partial y}\frac{\partial}{\partial z}(2.17) + \frac{\partial u}{\partial z}\frac{\partial}{\partial y}(2.16) - \frac{\partial b}{\partial x}\frac{\partial}{\partial z}(2.18) - \frac{\partial v}{\partial z}\frac{\partial}{\partial x}(2.16).\end{aligned} \tag{2.20}$$

So, we are not calculating PV in the exact Ertel sense, but instead we calculate a PV-like quantity for which a budget will more accurately close using ROMS diagnostic output. Writing

$$\frac{\partial \tilde{q}}{\partial t} = ADV + FRIC + DIA + PRES_{res} \tag{2.21}$$

T08 was able to calculate each of the terms *ADV, FRIC, DIA* and $PRES_{res}$ by inserting the right hand side of equations (2.16-2.18) into (2.20):

$$\begin{aligned} ADV = &\left(f + \frac{\partial v}{\partial x} - \frac{\partial u}{\partial y}\right)\frac{\partial}{\partial z}(ADVb) + \frac{\partial b}{\partial z}\frac{\partial}{\partial x}(ADVv + CORv) \\ &- \frac{\partial b}{\partial z}\frac{\partial}{\partial y}(ADVu + CORu) + \frac{\partial b}{\partial y}\frac{\partial}{\partial z}(ADVu + CORu) \\ &+ \frac{\partial u}{\partial z}\frac{\partial}{\partial y}(ADVb) - \frac{\partial b}{\partial x}\frac{\partial}{\partial z}(ADVv + CORv) - \frac{\partial v}{\partial z}\frac{\partial}{\partial x}(ADVb) \end{aligned} \tag{2.22}$$

$$\begin{aligned} FRIC = &\frac{\partial b}{\partial z}\left(\frac{\partial}{\partial x}(FRICv) - \frac{\partial}{\partial y}(FRICu)\right) \\ &+ \frac{\partial b}{\partial y}\frac{\partial}{\partial z}(FRICu) - \frac{\partial b}{\partial x}\frac{\partial}{\partial z}(FRICv) \end{aligned} \tag{2.23}$$

$$DIA = \left(f + \frac{\partial v}{\partial x} - \frac{\partial u}{\partial y}\right)\frac{\partial}{\partial z}(DIAb) + \frac{\partial u}{\partial z}\frac{\partial}{\partial y}(DIAb) - \frac{\partial v}{\partial z}\frac{\partial}{\partial x}(DIAb) \tag{2.24}$$

$$\begin{aligned} PRES_{res} = &\frac{\partial b}{\partial z}\left(\frac{\partial}{\partial x}(PRESv) - \frac{\partial}{\partial y}(PRESu)\right) \\ &+ \frac{\partial b}{\partial y}\frac{\partial}{\partial z}(PRESu) - \frac{\partial b}{\partial x}\frac{\partial}{\partial z}(PRESv). \end{aligned} \tag{2.25}$$

The $PRES_{res}$ term should be zero as it involves taking the curl of a gradient, but in the finite difference representation of the model, it may not come out to exactly zero.

T08 integrated equation 2.21 over a set of ROMS grid cells:

$$\int_V \frac{\partial \tilde{q}}{\partial t} dV = \int_V (ADV + FRIC + DIA + PRES_{res}) dV. \tag{2.26}$$

Since we're interested in the change in PV over the entire volume, we take the time-derivative outside the integral. Our control volume is bounded in the vertical by two

isopycnals, so the exact volume between those isopycnals will change over time. Thus, we must use the Leibniz theorem (Kundu, 2004):

$$\frac{d}{dt}\int_{V(t)} F(\mathbf{x},t)dV = \int_{V(t)} \frac{\partial F}{\partial t} dV + \int_{A(t)} F\mathbf{u}_A \cdot \mathbf{dA} \tag{2.27}$$

where $A(t)$ is the surface of $V(t)$ and $\mathbf{u}_A$ is the velocity of that surface. This formula states that the change in F over some changing volume V is equal to the change in F inside the volume plus the change in F due to the motion of the volume boundaries.

Equation 2.26 thus becomes

$$\int_{V(t)} \frac{\partial \tilde{q}}{\partial t} dV = \int_{V(t)} (ADV + FRIC + DIA + PRES_{res}) dV + \int_{A(t)} \tilde{q}\mathbf{u}_\mathbf{A} \cdot \mathbf{dA}. \tag{2.28}$$

We can define two ways the boundary of our control volume will change due to the motion of the isopycnals:

1) The particular cells contained within the volume will change as isopycnals move to include or exclude cells.

2) The cells themselves will change depth over time. Recalling the start of this chapter, there are 20 sigma levels regardless of the full water depth but the distribution of those levels *is* a function of depth. When the sea surface height changes, the depth of all the sigma levels also changes. We can view this phenomenon from the context of a change in sea surface height being distributed between all of the vertical cells, rather than just influencing the top cell.

The discretization of the model allows us to define the first of these terms quite easily.

$$\int_{A(t)} \tilde{q}\mathbf{u}_A \cdot \mathbf{dA} = \int_{A(t)} \tilde{q} \frac{dz_A}{dt} dxdy = \frac{1}{dt} \int_{V_A(t)} \tilde{q} dV_A = \frac{1}{dt} \left(\int_{V_i} \tilde{q} dV - \int_{V_e} \tilde{q} dV \right) V_i. \tag{2.29}$$

In the steps we have taken in 2.29, V_A represents the volume in the cells newly included in the control volume minus the volume in the cells newly excluded in the control volume, dz_A is the height of those cells. In the last step, we have separated the cells into the newly included volume V_i and the newly excluded volume V_e.

The second term is less straightforward. Contrary to the boundary motion term described above, the volumes newly included and excluded in this boundary motion term are not entire cells, but parts of cells. We can easily calculate the change in volume since dx and dy do not change and we have the depth of the cells at the and the new time steps. We do not know PV continuously across each grid cell, so to estimate the PV contained in this volume, we assume PV varies linearly across each grid cell. This calculation is performed along the top and bottom edges of cells in the control volume that are common to both the current and last time steps. This term is formulated in the same way as the first term; equation 2.28 now including the extra terms is:

$$\begin{aligned}\frac{d}{dt}\int_V \tilde{q}dV = &\int_V (ADV + FRIC + DIA + PRES_{res})dV \\ &+ \frac{1}{dt}\left(\int_{V_i} \tilde{q}dV - \int_{V_e} \tilde{q}dV\right) + \frac{1}{dt}\left(\int_{V_t} \tilde{q}dV - \int_{V_b} \tilde{q}dV\right)\end{aligned} \tag{2.30}$$

where V_t is the volume change due to the motion of the upper sigma surface and V_b the change in volume due to the motion of the lower sigma surface.

Various integrals in 2.30 are evaluated over different volumes, so it is helpful to back up a step and consider how the total PV contained in a volume is composed of the PV from various other volumes (rather than considering the time-derivative):

$$\int_{V'} \tilde{q}' dV = \int_V \tilde{q}dV + \int_{V_c'} \frac{\partial \tilde{q}}{\partial t} dtdV + \int_{V_i'} \tilde{q}' dV - \int_{V_e} \tilde{q}dV + \int_{V_{c,t}} \tilde{q}dV - \int_{V_{c,b}} \tilde{q}dV. \tag{2.31}$$

Here the ' represents a quantity calculated at time=t; anything without the ' represents a quantity calculated at time=t-1. The subscript *c* represents the cells common to both *V'* and *V*. Subscripts *i* and *e* mean as they did above, that we are integrating over only the cells that are newly included or excluded between the volumes *V* and *V'*. Similarly, subscripts *t* and *b* represent the volume that has been gained or lost due to the motion of the uppermost sigma surface and the lowest sigma surface, respectively. From left to right, we can interpret the terms in this equation as: the PV contained in the volume *V'* is equal to the PV contained in the volume *V* plus the change in PV in the cells common to *V* and *V'* plus the PV contained in the cells newly acquired in *V'* minus the PV in the cells newly lost from *V* plus the PV gained through motion of the uppermost sigma surface of the cells common to both *V* and *V'* minus the PV lost through the motion of the lowest sigma surface of cells common to both *V* and *V'*.

A 1-D example is shown in Figure 2.3. Equation 2.24 for this case would be

$$\begin{aligned}\tilde{q}_2'(z_3'-z_2')+\tilde{q}_3'(z_4'-z_3') = {} & \tilde{q}_1(z_2-z_1)+\tilde{q}_2(z_3-z_2)+\frac{\tilde{q}_2'-\tilde{q}_2}{dt}dt(z_3'-z_2') \\ & +\tilde{q}_3'(z_4'-z_3')-\tilde{q}_1(z_2-z_1)+\tilde{q}_{2.5}(z_3'-z_3)-\tilde{q}_{1.5}(z_2'-z_2)\end{aligned} \tag{2.32}$$

where the 1.5 and 2.5 subscripts denote values for q interpolated to the interfaces between cells (rather than values located at the centers of cells).

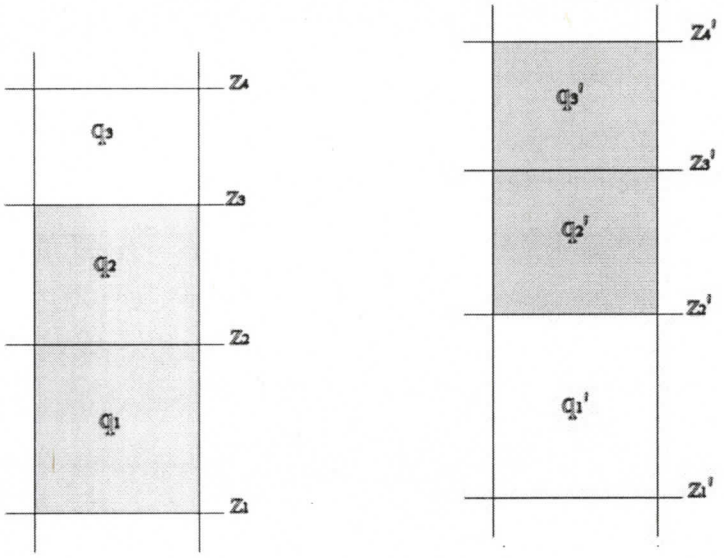

Figure 2.4 1 dimensional example of a PV budget; the left image shows the volume included in the budget at time t-1 and the right image shows the volume at time t.

Dividing equation 2.32 by *dt* gives:

$$\frac{1}{dt}\left(\int_{V'}\tilde{q}'\,dV-\int_{V}\tilde{q}dV\right)=\int_{V_c'}\frac{\partial\tilde{q}}{\partial t}dV+\frac{1}{dt}\left(\int_{V_n'}\tilde{q}'\,dV-\int_{V_o}\tilde{q}dV\right)+\frac{1}{dt}\left(\int_{V_{c,t}}\tilde{q}dV-\int_{V_{c,t}}\tilde{q}dV\right). \tag{2.33}$$

The left hand side is now the (discretized) derivative we are looking for. Finally, we may substitute in equation 2.26 for the first term on the right hand side:

$$\frac{1}{dt}\left(\int_{V'}\tilde{q}'\,dV-\int_{V}\tilde{q}dV\right)=\int_{V_c'}\left(ADV+FRIC+DIA+PRES_{res}\right)dV+\frac{1}{dt}\left(\int_{V_n'}\tilde{q}'\,dV-\int_{V_o}\tilde{q}dV\right)+\frac{1}{dt}\left(\int_{V_{c,t}}\tilde{q}dV-\int_{V_{c,b}}\tilde{q}dV\right). \tag{2.34}$$

Equation 2.34 is the final equation used for the PV budget.

Discretization required some spatial averaging. Derivatives were centered at the middle of each grid cell, known as the ρ-point. ROMS uses an Arakawa C-grid (Arakawa and Lamb, 1977), so it was necessary to average various variables to the appropriate coordinate system. For example, the derivative of v with respect to x required knowledge of v at u-points; this was attained by averaging the four values for v surrounding the appropriate u-point.

Some time-averaging was also required. Diagnostic data was output at times between instantaneous data so the latter were averaged to get them to the same times as the diagnostic data. Time derivatives were centered.

In the case where the control volume included land-masked regions, the masked grid cells as well as the cells directly adjacent to the masked cells were not included in the calculation. This procedure was due to the model's practice of outputting zeros for all values within masked regions. Many of the quantities calculated by the budget require values from adjacent grid cells, which necessitated exclusion from the budget of the cells directly adjacent to the masked cells. It is assumed that while these cells probably contain valuable information, the next layer of cells away from the shore – in which the budget *has* been calculated – contains a similar signal.

The budget was performed on a sample region over two days to test its validity, the results of which are shown in Figure 2.5. The rms difference between the left- and right-hand sides (ie the black and the blue lines, respectively) of equation 2.34 in this case is 0.0098.

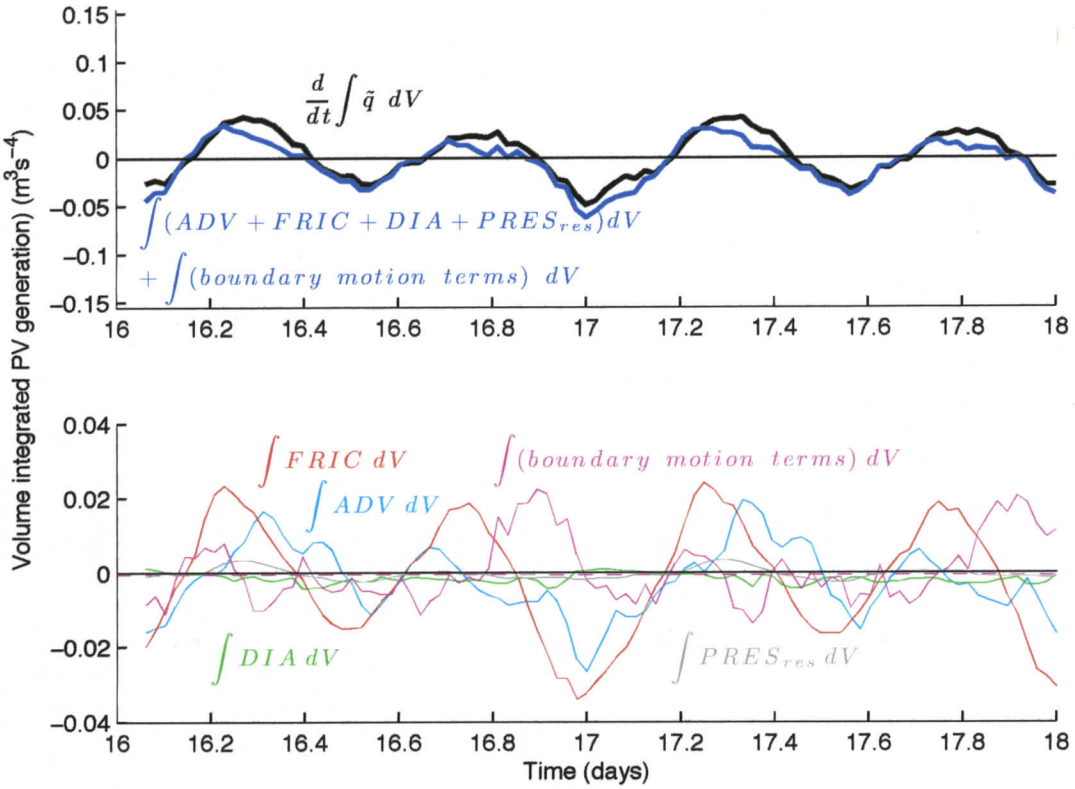

Figure 2.5 Equation 2.34 is calculated over a 30x25 set of cells near Cape St. James between the surface and ρ = 26 (this is the "generation region" discussed in chapter 4). The black and blue lines in the upper panel are the left and right hand sides of equation 2.34 respectively, the various coloured lines in the lower panel are the terms in the right-hand side of equation 2.34. The root mean square of the difference between the black and blue lines is 0.0098.

The lines in Figure 2.5 can be interpreted in the following way: friction generates positive and negative PV as the tide moves back and forth with a 12-hour period. Generation due to mixing is negligible in this region. Advection is cyclical and roughly follows the friction term. However, instead of a negative value meaning advection of negative PV into the box, it generally means advection of positive PV *out* of the box (at least for this region, which we will show in chapter 4 as being the primary PV generation region). Tides can also be seen in the boundary motion terms: similar to the advection term, a positive signal may mean either the inclusion of new volume with positive PV or

the exclusion of volume with negative PV. However, the fact that the signal is comparable in size to the other terms indicates large tidal amplitudes.

All of the terms have some error associated with the time discretization. The model has a time-step of 40 seconds but only outputs data every 30 minutes, so time derivatives calculated here are not quite the same as those calculated within the model. This type of error will be most prevalent at times when there is the greatest variability occurring between time-steps, which likely explains the increase in error at times of largest PV generation, which will coincide with the largest current speeds. In addition, there is some error in the second boundary motion term since the assumption of a linear variation of PV between grid cells is certainly false.

3. Description of Results

The primary process discussed in this chapter is the generation of eddy dipoles at Cape St James and their evolution over the 48 days of the model run. Small (~3 km radius) dipoles are initially generated at the cape, some of which migrate into a "coalescence zone" where they merge with previously generated eddies. We are then left with a pair of counter-rotating eddies larger (~16 km radius) than those originally generated at the cape. Every 15 days these eddies drift into deeper water and a new set forms. Figure 3.1 shows an example of this eddy dipole after it has moved offshore, from day 31 of the model run.

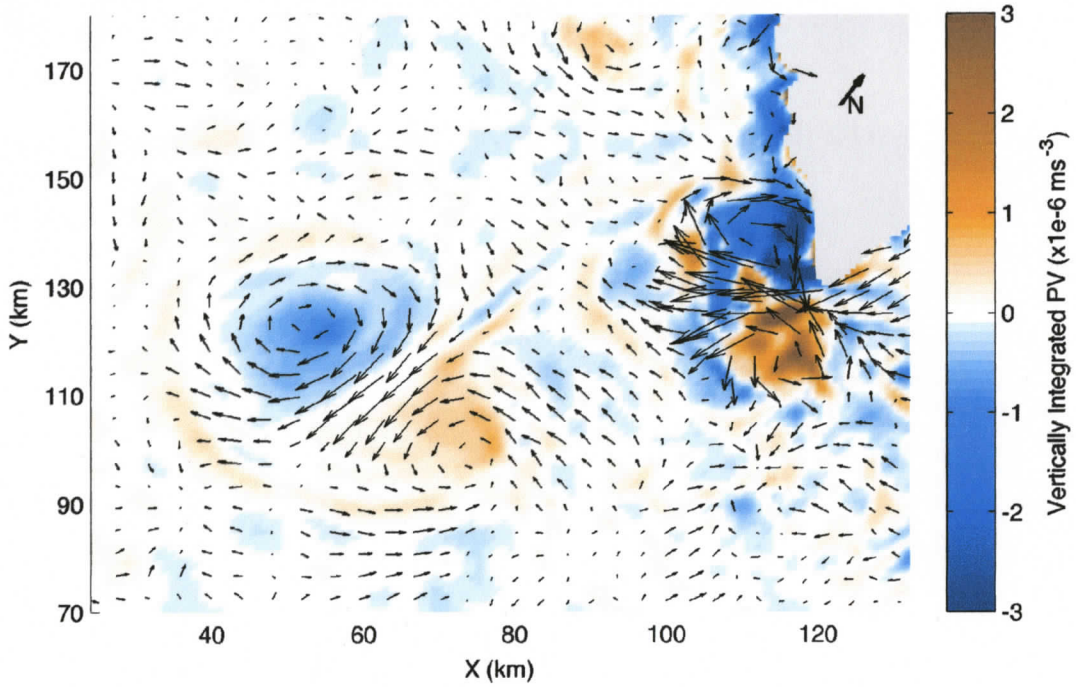

Figure 3.1 Examples of a fully formed dipole and a newly forming dipole are shown in this image of vertically integrated potential vorticity[1] on day 31 of the model run.

This chapter breaks down the evolution of these eddies in a strictly descriptive sense; discussion of the mechanisms behind each process is left for the next chapter.

[1] All figures showing vorticity or potential vorticity have neglected any contribution from f so that an equality of dipoles can be assessed.

3.1 Generation of Potential Vorticity

Potential vorticity (PV) generation at Cape St James occurs alternately on the ebb (producing a clockwise circulation, i.e. containing negative vorticity) and the flood tides (counterclockwise circulation, i.e. containing positive vorticity). This generation is tracked in Figure 3.2 where vertically-integrated PV near the cape is shown every two hours starting at a flood tide; the inset plot is of the cross-shelf barotropic velocity averaged over the same region. In hour 1, there is a small (radius of ~3 km) patch of positive PV (red) forming on the east side of the cape during a flood tide. When the tide begins to ebb in hour 5, this patch is advected westward and negative PV (blue) is generated on the west side of the cape, although this generation is not nearly as clear as the positive PV generation due to the lingering presence of negative PV in the region from previous ebbs. During the following flood in hours 11 and 13, the red patch generated in hour 1 is advected back eastward and a new red patch is also formed to the east of the cape. The two red patches merge (hours 13-17) and the following ebb advects them both well away from the cape. This ebb also generates more negative PV, but again, it is difficult to track. We will continue to track the positive PV eddies to obtain some sense of their fate.

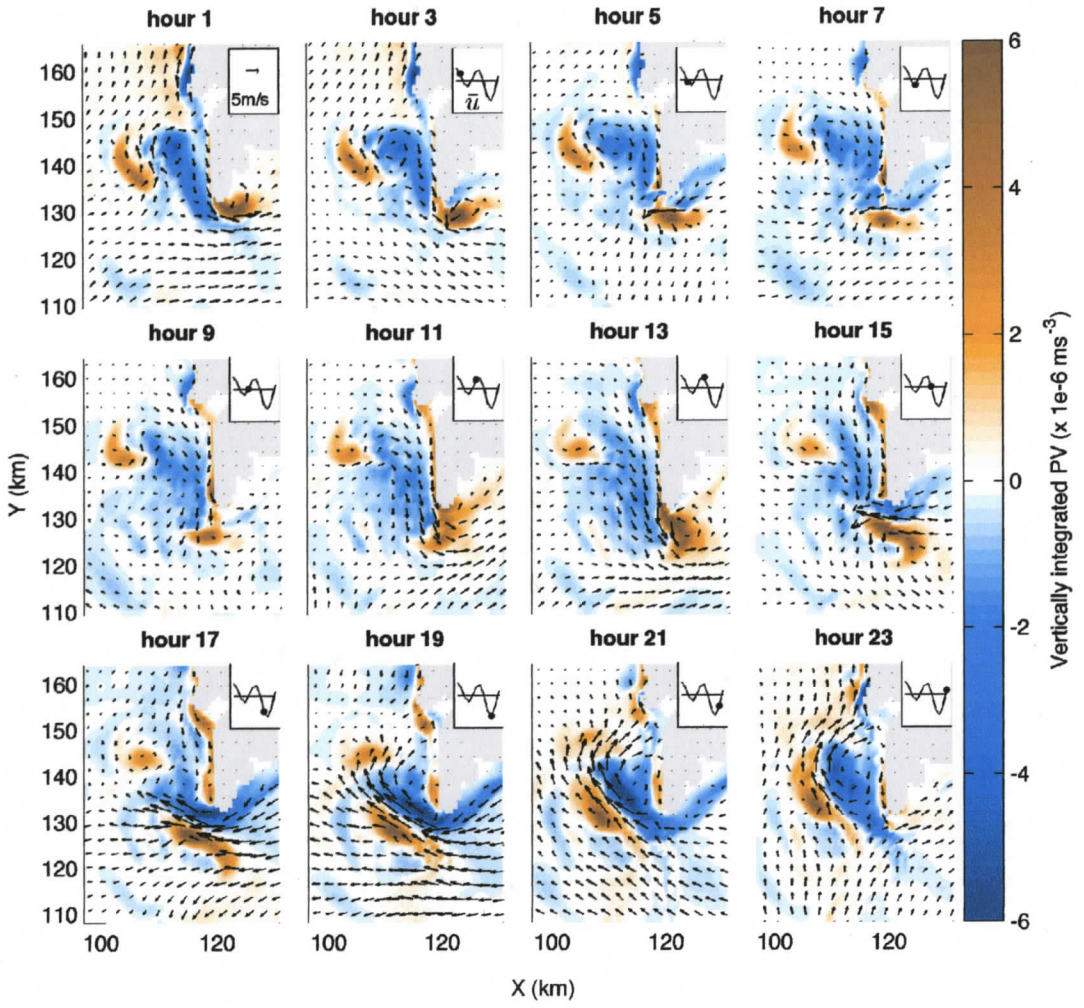

Figure 3.2 Evolution of potential vorticity over the course of day 13. The PV shown here is integrated between the isopycnals ρ_1=0 kgm^{-3} and ρ_2=26 kgm^{-3}; velocity arrows are interpolated to 50m depth. The inset shows cross-shelf velocity averaged over the same region.

3.2 Tracking the positive PV eddies

There are four possibilities for the fate of the positive PV eddies (as noted above, the negative PV eddies generated at the cape are more difficult to track so we assume their advection tracks break down into a similar range of options). Which track an eddy follows depends on the strengths of the generating flood and the ebb that follows this

generation. Each case is indicated as a cartoon in Figure 3.4, with examples in Figures 3.2 and 3.3.

A. Any flood/strong ebb (ex. eddy surrounded by the medium grey box which starts at the cape in hour seven of Figure 3.3; panel A in Figure 3.4): the strong ebb advects the eddy well west of the cape; subsequent ebbs push the eddy further north. These eddies appear to coalesce about 50 km north of the cape, creating a stationary (at least over the course of the 48-day model run accomplished here) dipole feature; an investigation of this feature was beyond the scope of this analysis.

B. Weak flood/weak ebb (ex. eddy which starts at the cape in hour one of Figure 3.2; panel B in Figure 3.4): the eddy remains close enough to the cape that the following flood pushes it back into the generation region where it joins with the new eddy generated on this flood. The fate of this new eddy is then governed by the generating flood and following ebb (weak flood – weak ebb will always be followed by strong flood – strong ebb, ie case A).

C. Strong flood/medium ebb (ex. eddy bounded by the black box which starts at the cape in hour one of Figure 3.3; panel C of Figure 3.4): the strong flood pushes the eddy out of the way of the strong tidal currents near the cape and the following medium ebb advects the eddy out of the generation region, into a "coalescence zone". Since the tidal currents in this region are relatively weak, eddies tend to stay here, joining with any other eddies entering the region.

D. Very weak flood/any ebb (ex. eddy bounded by the light grey box which starts west of the cape in hour one of Figure 3.3; panel D of Figure 3.4): an especially weak flood generates too little PV to have lasting meaning in the domain, regardless of the strength of the following ebb.

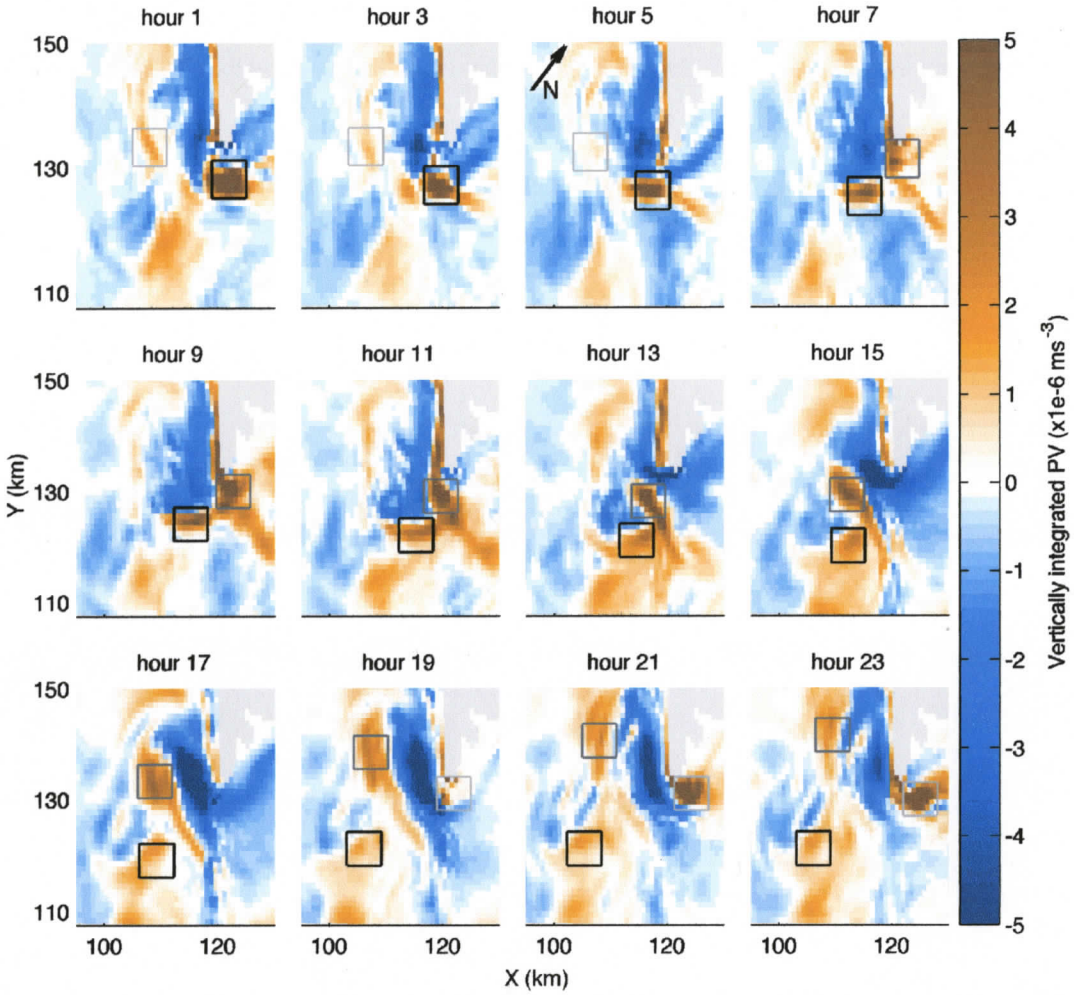

Figure 3.3 PV vertically integrated between ρ_1=0 kgm^{-3} and ρ_2=26 kgm^{-3} for day 17. Boxes indicate eddy tracks for various positive PV eddies. An example of a coalescing eddy can be seen by following the black boxes which start at the cape in hour 1.

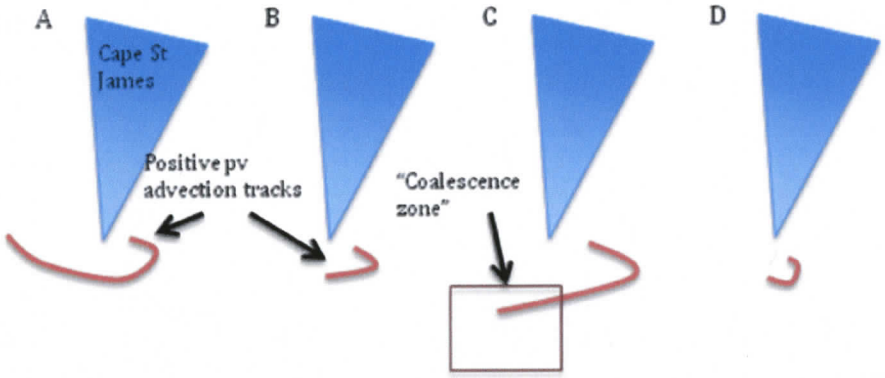

Figure 3.4 Cartoon of various possible advection tracks for positive PV eddies from the start of the generating flood to the end of the next ebb. Refer to the text for a description of each panel.

Other combinations of strong and weak ebbs and floods are possible, but the short duration of the model run means that the strength of the ebbs and floods were ordered the same through each of the three spring-neap cycles, as there wasn't time for significant differences to emerge. Between neap and spring tide of this run, the ordering of tides was a strong flood – strong ebb – weak flood – weak ebb; between spring and neap tides, there was a strong flood – weak ebb – weak flood – strong ebb cycle. This cycle is shown in Figure 3.5 where the cross-shelf barotropic velocities averaged over a small region just south of the cape are shown between the second and third neap tides of the model run.

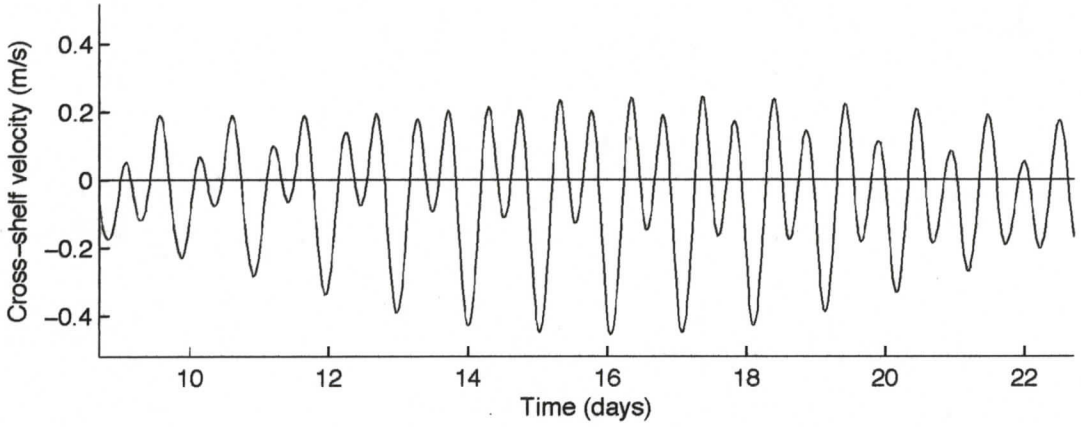

Figure 3.5 Cross-shelf barotropic velocity averaged over a small (20 km x 20 km) region south of Cape St James

Another way to separate the different tracks of positive PV eddies is to look at the location of the eddies at the end of the generating flood and again at the end of the following ebb. Figure 3.6 shows these locations between the second and third neap tides; different markers are used to associate the final fate of each eddy type. Of particular interest are the locations of the stars (case C - coalescing) compared to the other symbols – at the end of the ebb following the generating flood, they are grouped well away from the cape where they stay to coalesce with subsequent eddies advected there. This particular combination of strong flood/medium ebb occurs every other tidal cycle between spring and neap tide for this particular run (Figure 3.5) although, as noted above, if the model run were to go longer, the tidal constituents would have different relative phases so the ordering of strong and weak ebbs and floods would vary.

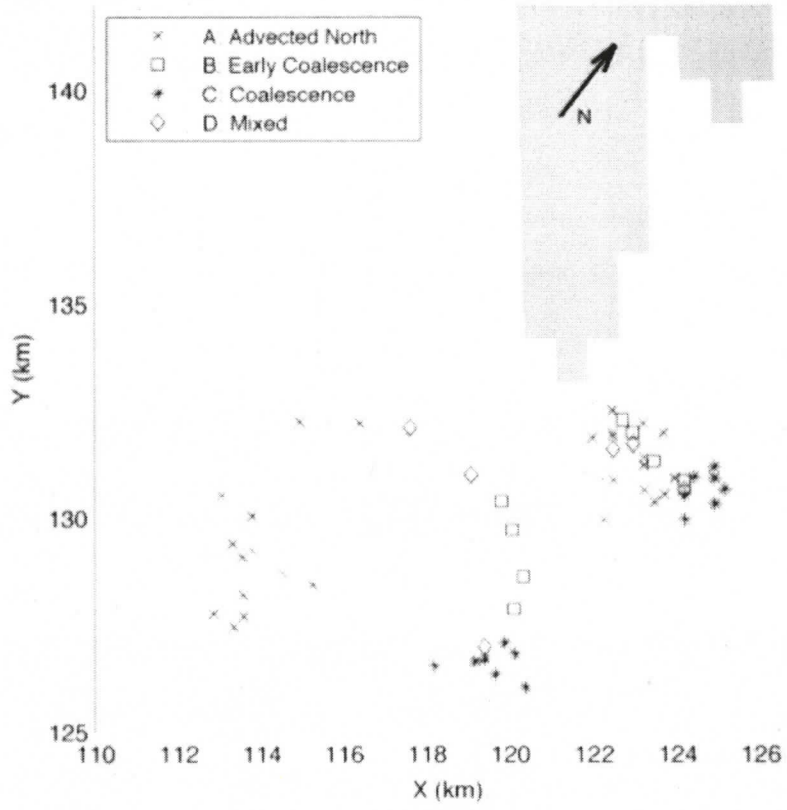

Figure 3.6 The location of the positive PV eddies at the end of the generating flood and the following ebb, marked according to their final fate: advected north (crosses); returning to the generation region to coalesce with the eddy generated on the next flood (squares); coalescing with other positive PV eddies south of the cape (stars); mixing with negative PV (diamonds).

The feature of interest to this study is generated by those eddies which merge in the coalescence zone (case C). In each spring-neap cycle there are 5-7 positive PV eddies which coalesce. There are usually 1-2 more which enter the coalescence zone before the others, but these quickly mix with the negative PV in the region and so don't contribute towards forming the final large eddy. The first eddy marked as a coalescing eddy mixes slightly, but stays intact for the most part. Each subsequent eddy which enters the coalescence region interacts with the eddies already present, deforming and wrapping around each other until a single, larger (~12 km radius), eddy is formed. An example of the path an eddy takes to coalescence is shown in Figure 3.3 where positive PV eddies

are tracked on day 17 of the model run; the black boxes which start at the cape in hour 1 track an eddy to its coalescence with the larger feature in hour 23.

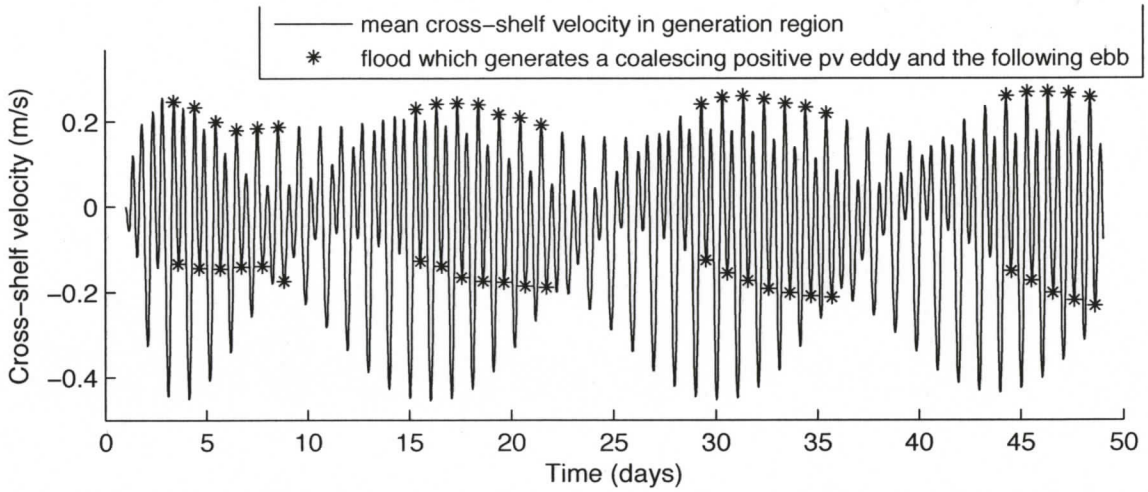

Figure 3.7 Cross-shelf barotropic velocity averaged over a small (20 km x 20 km) region south of Cape St James with markers showing the generating flood and following ebb for coalescing eddies (tidal velocities over the first day are unusually low because there is a one day ramp-up of tidal forcing in the model).

Although we do not track specific patches of negative PV from the cape to the coalescence zone, a large negative PV feature emerges in this region next to the positive PV feature, growing at a similar rate. Thus, a large dipole is produced to the west of the cape due to coalescence of small eddies generated at the cape.

3.3 Large-scale Evolution

The large dipole discussed in the previous sections absorbs PV generated at the cape and drifts into the deep water offshore allowing a new dipole to form at the cape. Figure 3.8 shows days 3 through 48 of the model run, marking the dipoles from the first through fourth cycles; the dipole at the cape grows with time until it detaches from the cape between days 6 and 9, to drift southwestward. A new dipole begins to form at the cape soon after. In the case of the second cycle, the large dipole stays close enough to the cape

that it absorbs the detached PV from the third cycle (between days 36 and 39) before continuing southward and a fourth cycle begins.

A discussion of the large feature about 50 km up the western coast of Haida Gwaii is beyond the scope of this research. However, it likely evolves from the PV that is generated at the cape but not contained there (case A from section 3.1).

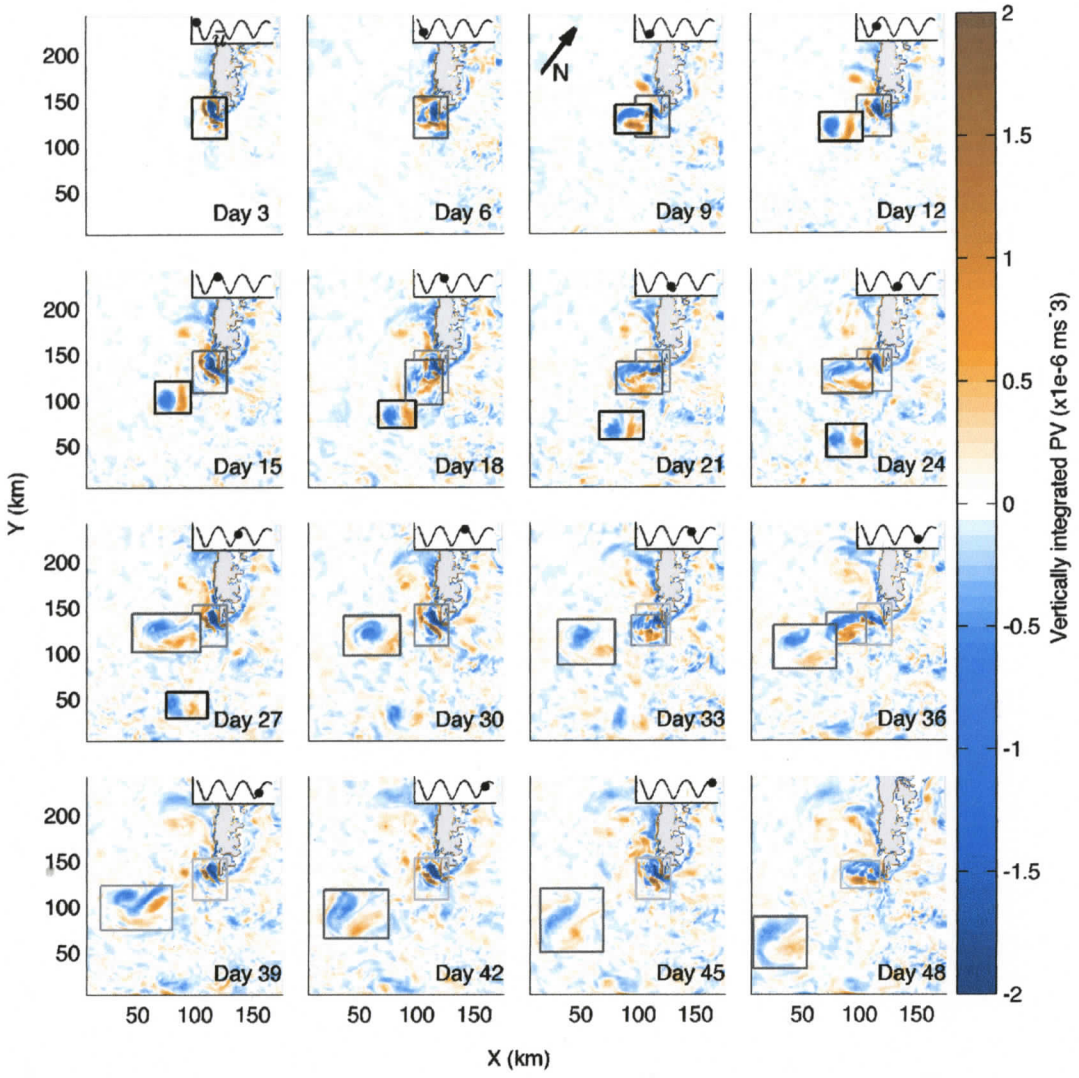

Figure 3.8 Evolution of potential vorticity integrated between ρ_1=0 kgm^{-3} and ρ_2=26 kgm^{-3} from day 1 to day 46. Each box encloses a large dipole with different box shades indicating different dipoles. The box for the first dipole is only drawn until day 27; after this point the dipole was affected by the proximity of the model boundaries. The inset in each pane of the figure shows cross-shelf speed averaged over 4 days to extract the spring-neap cycle of the tide.

A dipole representative of those that have detached from the cape and started drifting southward is shown in Figure 3.9. This figure is generated from a six-hour average of all fields to remove the background tidal signal. The dipole is from day 31, so it was

generated during the second cycle, prior to merging with the third dipole. The clockwise (counter clockwise) eddy has a diameter of approximately 30 km (25 km) and extends to 100 m (150 m) depth; with these dimensions, the total volume of each eddy is close to 7e10 m^3. Velocities reach up to 20 cm/s in each eddy. The dipole travels southwestward at a rate of 6 km/day (calculated from the motion of the dipole in the first cycle as it is the only one to move a significant distance in the length of the model run). While the density within the clockwise eddy is approximately constant at this depth, there is upwelling of isopycnals within the counter clockwise eddy.

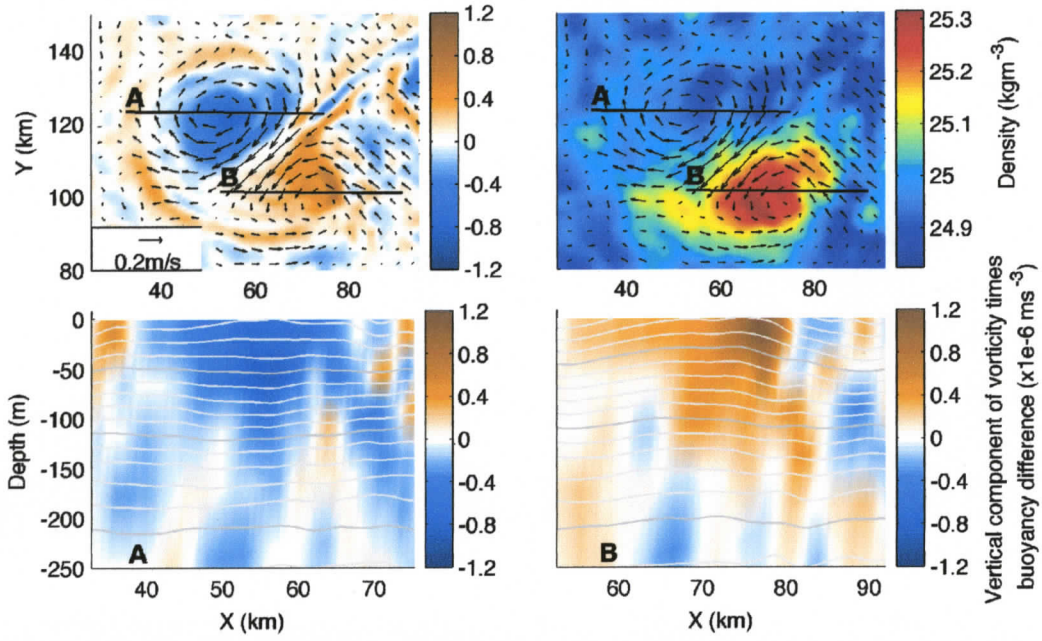

Figure 3.9 The eddy pair at day 31 (from cycle 2, prior to merging with the eddy pair in cycle 3). The upper left image shows a plan view of the vertical component of vorticity[2] at 50 m depth with velocity arrows; the upper right image shows density at the same location. The lower images are transects of the same vertical component of vorticity at the locations indicated by the lines 'A' and 'B' in the upper images. Each of the lower images has density contours every 0.2 kg/m^3; the darker grey lines are shown at 25, 26, and 27 kg/m^3.

In the second and third cycles, the dipoles merge, the results of which are shown in Figure 3.10. The extent of the positive PV eddy appears to have shallowed to ~100 m,

[2] Previous figures have shown vertically integrated potential vorticity between the surface and ρ=26 kgm^{-3}; since we are showing a vertical slice in Figures 3.9 and 3.10, a vertically integrated quantity would not be possible. Instead we show the vertical component of vorticity scaled by the difference in buoyancy between the surface and the ρ=26 kgm^{-3} isopycnal. For vertically uniform PV which is oriented principally in the vertical, the two quantities are equivalent. The surface density was chosen as ρ=24.5 kgm^{-3} which is approximately the average surface density in the region.

while the negative PV eddy continues to extend to 100 m depth as well. Both eddies have grown to ~40 km diameter, giving a total volume for each eddy of ~1e11 m^3.

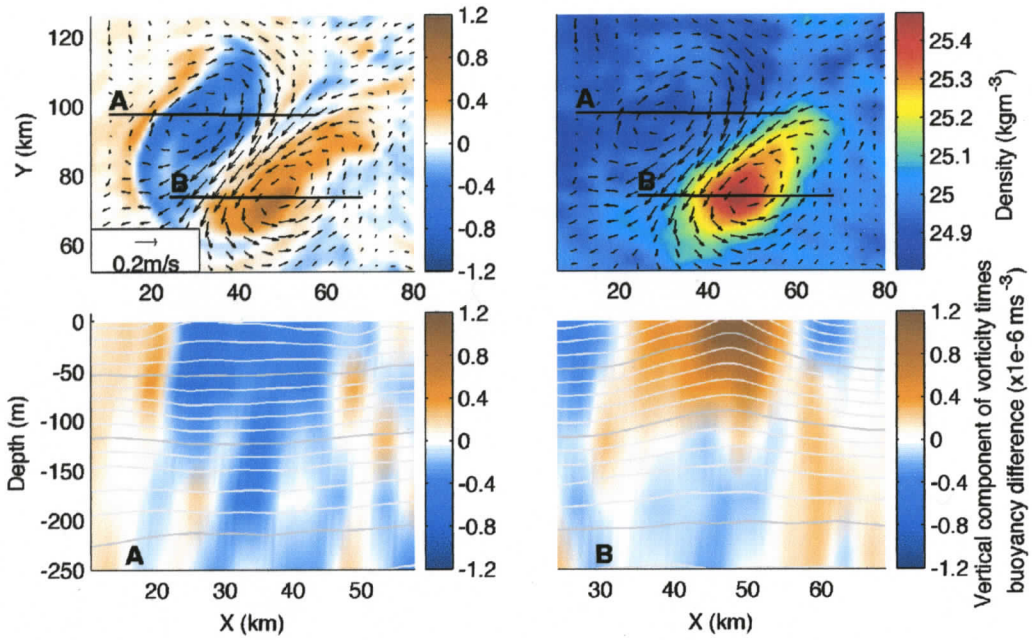

Figure 3.10 The eddy pair at day 42 (after the merging of the eddy pairs from the second and third cycle). The upper left image shows a plan view of the vertical component of vorticity[1] at 50 m depth with velocity arrows; the upper right image shows density at the same location. The lower images are transects of the same vertical component of vorticity at the locations indicated by the lines 'A' and 'B' in the upper images. Each of the lower images has density contours every 0.2 kg/m^3; the darker grey lines are shown at 25, 26, and 27 kg/m^3.

4. Analysis of results

In the previous chapter we took a qualitative look at the generation of mesoscale eddies from the merging of small headland eddies. Here we quantify this process, looking at what mechanism generates the little eddies and where exactly this occurs. We also consider how efficiently these eddies are generated and how efficiently they merge into the larger eddies.

4.1 Frictional generation of positive PV

The PV in the headland eddies is generated by friction at Cape St. James. As noted in chapter 2, PV can be generated through mixing or friction – Figure 4.1 shows that frictional generation of PV vastly exceeds that generated by mixing. Frictional generation closely follows the cross-shelf velocity with positive PV being generated on the flood tide and negative on the ebb; the strength of the tide (line in upper panel) is directly related to the amount of PV generated (black line in lower panel). The difference between the frictional generation (red line) and the change in PV (black line) is advection of PV out of the region. This is most notable during strong ebbs where PV is being advected offshore, west of the cape. What we have defined as the "generation region" is shown by the black box in Figure 4.2.

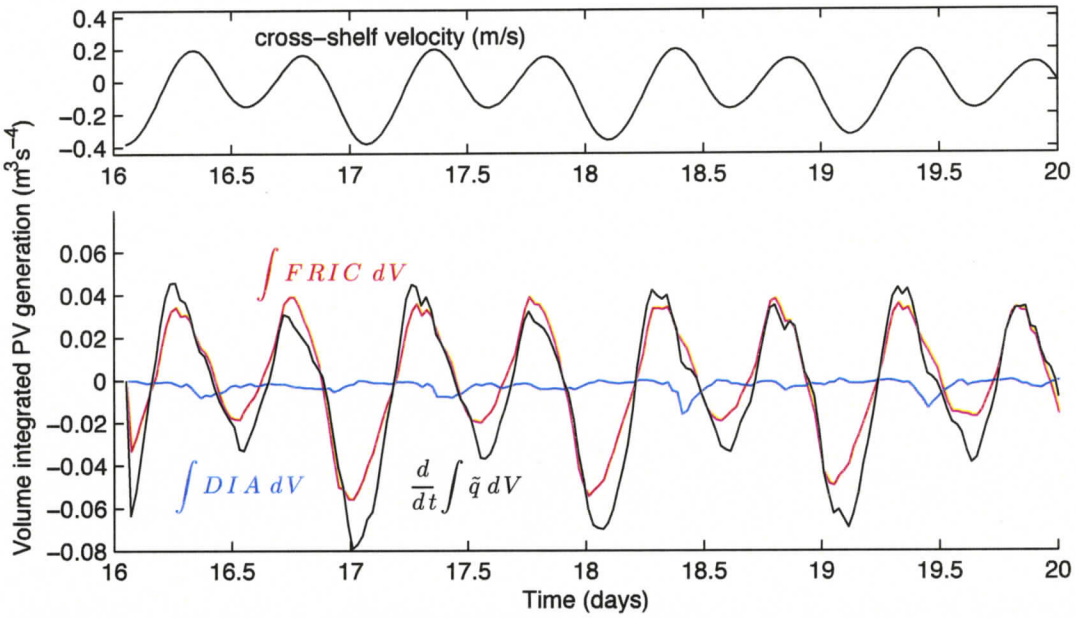

Figure 4.1 Potential vorticity generation due to mixing and due to friction for a region 20 km by 20 km centered near Cape St James (region is shown in Figure 4.2) for days 16-19 of the model run. Frictional generation greatly exceeds generation via mixing and dominates the change in PV for the region. The total change in PV was calculated as the sum of the generational terms rather than directly calculated as the change in PV. This difference is noted in chapter 2 as having a small associated error (see Figure 2.5 for all of the terms in the budget for days 16 and 17 only).

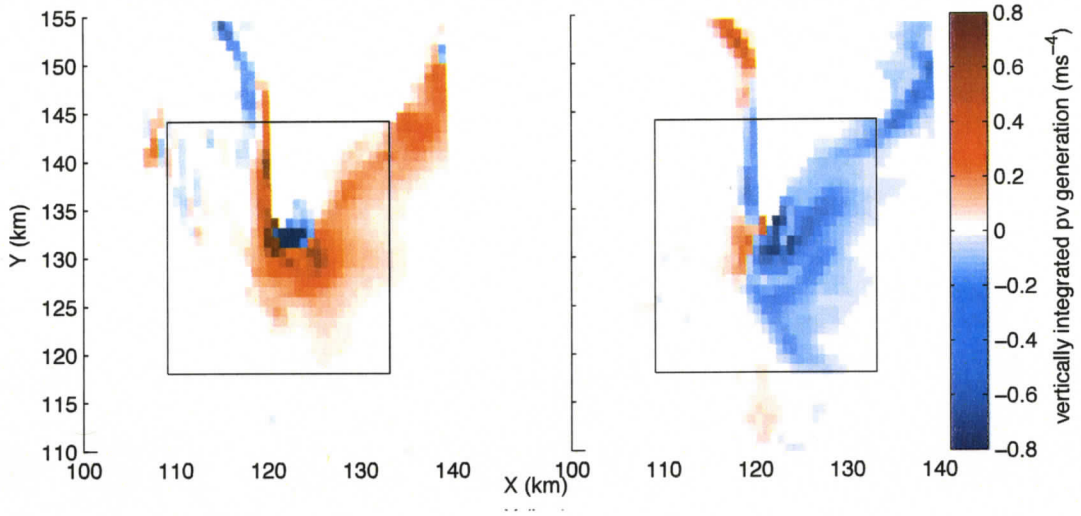

Figure 4.2 The black box denotes the region primarily responsible for generating the potential vorticity seen in the eddies. The colours represent vertically integrated (over the full depth) PV generation by friction during times of maximum positive (left panel) and negative (right panel) generation. The blue patch of negative PV seen in the middle of the positive PV in the left panel is characteristic of the return flow of the positive PV eddy – the westward flow across the cape generates negative PV in the same fashion as an ebb tide; this occurs frequently on both flood and ebb.

The net advective term is small compared to the frictional generation (Figure 4.1). However, we also need to show that the flux of PV through each wall is small to prove that large amounts of PV are not being generated outside the box and simply advected through the box to the other side. There is obviously generation of PV outside this box (Figure 4.2), most notably up the east and west coasts north of the box, however the flux of PV through any side of the box is negligible compared to the frictional generation inside the box (Figure 4.3). Advection of negative PV through the eastern boundary (purple line in the upper panel of Figure 4.3) is in phase with the negative PV generation (black line in the upper panel) as would be expected since an ebb tide will both generate negative PV, and advect into the box negative PV generated east of the box. Before day 17 (~spring tide), outward advection of both positive and negative PV occurs through the north and northwest boundaries; after this time, advection through the south and southwest boundaries increases. This is consistent with our description in the previous

chapter of coalescing eddies being generated after spring tide and northward advecting eddies being generated before.

Any conclusion we make about the negative PV signal based on distinguishing between advection out of the south and southwest boundaries vs the north and northwest boundaries must be made with reservation. The split between the northwest and the southwest boundaries was based on the positive PV eddy tracks and we do not know with certainty that the advective tracks of the negative PV eddies will split at the same location. However, it does appear that negative PV is advected northward before spring tide and south or west after spring tide, as with the positive PV. Given that the negative PV eddy in the final mesoscale dipole is the same size as the positive PV eddy (Figure 4.6), it seems likely that a similar number of negative PV headland eddies coalesce as those containing positive PV eddies.

For Figure 4.3, and many of those following, PV has been separated into positive and negative values. This was done partly to see if equal amounts of positive and negative PV were generated, and later contained, in the eddy dipoles, but also because the small eddies containing positive PV were much more easily tracked than those containing negative PV; many plots and calculations done with the small eddies were done only using the positive PV eddies. Splitting generation into positive and negative values allows us to compare how much PV is generated to how much is contained in an eddy.

Frictional generation in Figure 4.3 is a net value over the whole generation region: the entire PV field is integrated over the volume at each time-step. If the result is negative, it is considered negative generation, similarly for a positive result. The positive and negative results are then integrated over time separately. Advective values in this figure are not net values over the boundary in question, but rather considered on a point-by-point basis: for each time-step, the positive and negative fluxes are separated and integrated over each boundary separately.

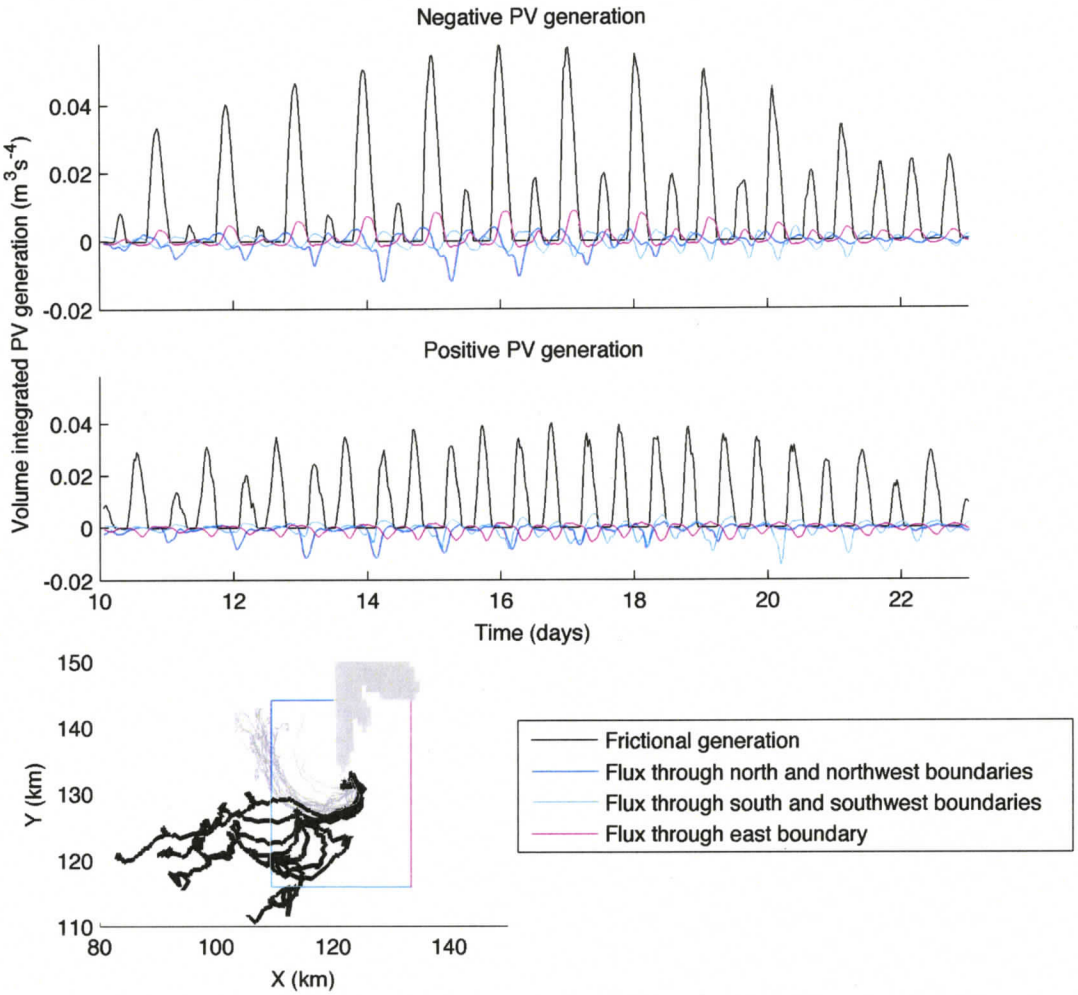

Figure 4.3 A comparison between the frictional generation of PV inside the box shown in Figure 4.2 and the advection of PV through the sides of the box. We have separated the western boundary of the box as shown in order to distinguish between eddies that advect northwards (ie pass through the northern boundary or the northern half of the western boundary) from the eddies that coalesce (these advect out of the box via the southern boundary or the southern half of the western boundary). This separation is indicated by the map in the lower left corner, showing the positive PV eddy tracks between the first and second neap tides (ie generated in the time period shown in the upper panels). From this figure, we can see that to within approximately 10% error, we can ignore the advective terms as a source of potential vorticity. See text for a full description of how the split between positive and negative generation and advection was achieved.

4.2 Efficiency of PV generation

We have now shown that the region responsible for generating the eddies is enclosed by the box shown in Figure 4.2. However, this region actually generates about twice as much PV as is accounted for by the headland eddies. The amount of PV generated on each flood tide is shown in Figure 4.4 and the amount of PV contained in each positive PV eddy at the end of the generating flood is shown in Figure 4.5; only about 40% of the vorticity generated is put into generating eddies (Table 4.1). The rest is likely lost due to mixing with negative PV in the region while some advects elsewhere to mix or form other features; the latter is a comparitively small amount, as advection of PV out of the generation region is small compared to how much is generated (Figure 4.3).

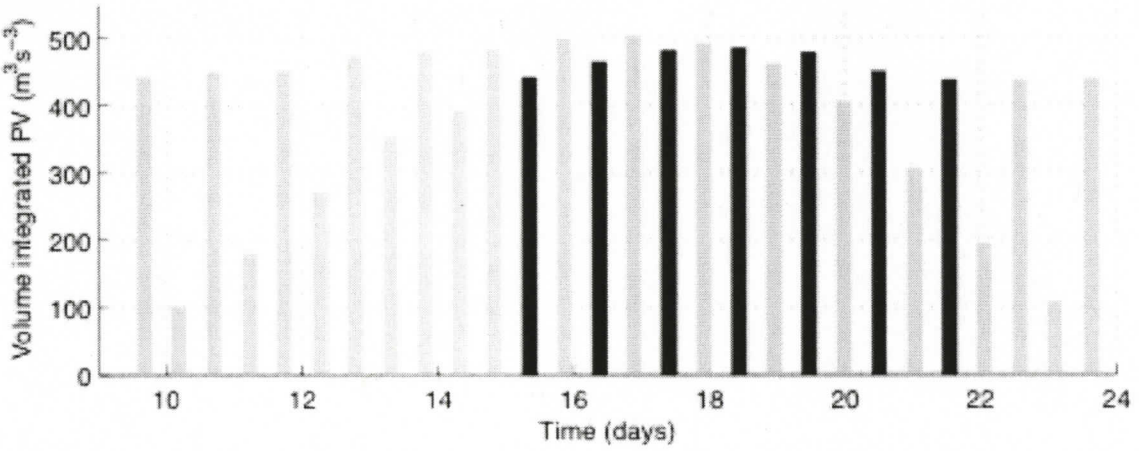

Figure 4.4 Positive PV generated by friction on each flood tide between the first and second neap tides in the generational region shown in Figure 4.2. Bars shown in black indicate eddies which coalesce, for easy comparison to lines in Figure 4.5.

The calculation of how much PV is contained within each of the small eddies required some art. The centre of the eddy was tracked; the eddy bounds were approximated by extending a 6 km by 6 km box around the centre which extends the full water column (these boxes were plotted in Figure 3.7). We then integrated the PV over this box. In performing this calculation, there were (rare) occasions where the boxes surrounding two eddies would overlap. To avoid over-counting the PV contained in the boxes in these

instances, the overlapped region was considered to be only part of the first eddy generated.

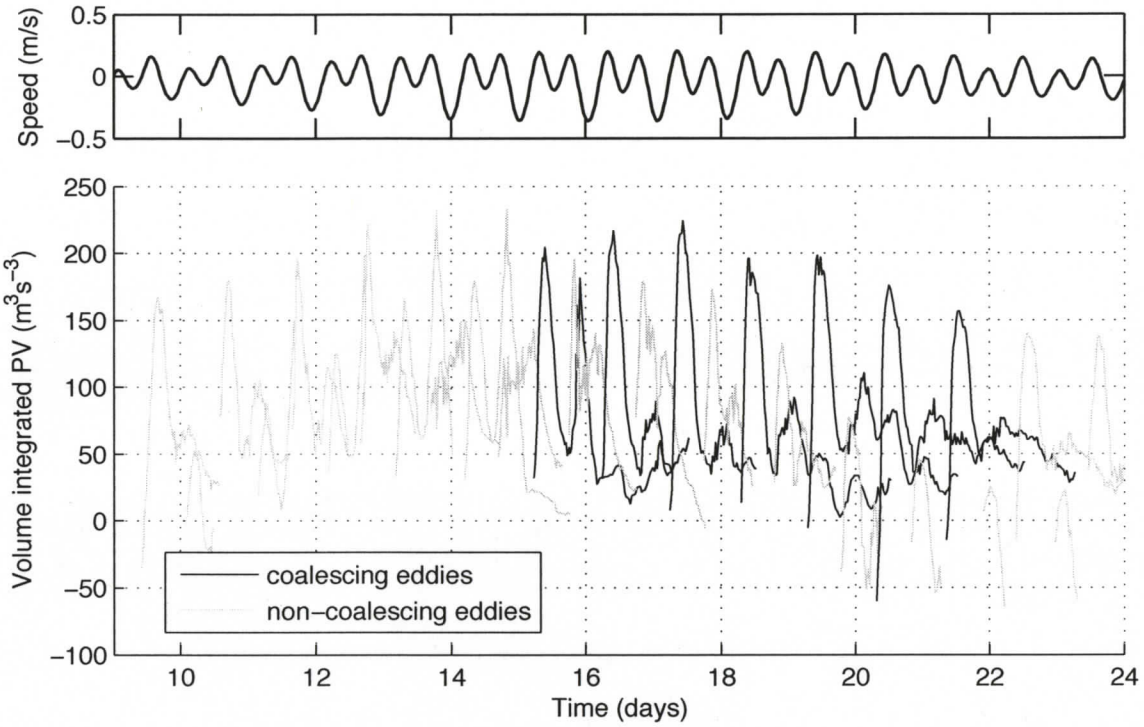

Figure 4.5 Volume-integrated potential vorticity contained in each positive PV eddy generated between the first and second neap tides. Each eddy was tracked until it became obvious which direction it was heading, so some eddies are tracked longer than others. The eddies which eventually coalesce to form the feature of interest are shown in black, all other eddies are shown in grey. The cross-shelf tidal velocity is shown in the upper panel; we can see here that the eddies which coalesce are generated on a strong flood tide which is followed by a weak ebb.

Each eddy-generation in Figure 4.5 follows a similar pattern which we can understand by referencing the vertically integrated PV of day 17 in Figure 3.3. The black box nearest the cape in hour one of that figure corresponds to the peak of the third black line in Figure 4.5. In the ebb between hours one and seven, the PV in this box mixes with surrounding negative PV which explains the drop off in PV shown in Figure 4.5. Then, in hours 9 to 15, frictional generation pumps more PV into the eddy. Near hour 15, the eddy has begun to merge with previously generated eddies. The box we are using to

represent the eddy is not without fault, as shown by Figure 3.3. The eddy changes shape slightly such that the box does not accurately contain it, and diffuses outside the box over time. The box also occasionally contains a small part of the adjacent negative PV feature. All of these concerns combine to make the values shown in Figure 4.5 low approximations.

The efficiency of friction at generating positive PV eddies is estimated by comparing the PV contained in an eddy at the end of the generating flood to the PV contained in the eddy at the end of the following ebb. This efficiency rating is a measure of how much the eddies mix with surrounding negative PV over the six hours of the ebb. This value is used since the PV in the eddy becomes reasonably stable after this point, although a bit more PV is pumped in on the next flood and the eddy diffuses somewhat outside the box, increasing the error in the volume-integrated PV calculation. The PV contained in each of the coalescing eddies at the end of their generating floods (ie at the first maxima for each line in Figure 4.5) and at the end of the following ebb (ie the first minima in Figure 4.5) is shown in columns two and four of table 4.1. The average efficiency of friction at generating positive PV eddies is 21%.

Positive PV generated by friction in the "generation region"	PV contained in positive PV eddies at the end of the generating flood	Fraction of frictional generation aimed at generating eddy	PV contained in positive PV eddies at end of ebb	Efficiency of friction at generating positive PV eddies
443	204	0.46	49	24%
469	217	0.46	34	16%
485	225	0.46	35	16%
484	196	0.41	34	17%
477	199	0.42	50	25%
449	176	0.39	36	20%
439	157	0.36	45	29%

Table 4.1 A summary of the efficiency of friction at generating positive PV eddies in this region. See text for a full description of the data shown here.

An efficiency rating can also be calculated for the merging of small positive PV eddies to form the large positive PV eddy. There are a total of seven small eddies which coalesce to form the larger eddy (Figure 4.5); this particular eddy is part of the second dipole formed in the model run. The total PV in each large dipole is shown in Figure 4.6 where we have integrated the PV over boxes containing each large dipole (these boxes were shown in Figure 3.8). These boxes do change volume over time simply because the dipole disperses somewhat, growing horizontally. It was not possible to define a box of constant volume due to the large amount of variability seen, particularly near the cape. The results are shown in Figure 4.6 where we have highlighted the second dipole in red for further study. Since the box initially includes the generation region at the cape, the total PV in the box is anomalously large for the first ~eight days. After this point the dipole (and thus the box) move away from the cape. At this point, the total positive PV contained in the box stabilizes to approximately 400 m^3s^{-3}.

To obtain an efficiency for the merging of the small eddies, this sum is compared to the sum of the PV contained in the small eddies prior to coalesence. If we estimate the PV contained in the seven small eddies prior to their coalescence as being 70 m^3s^{-3}, we find that we started with ~490 m^3s^{-3}. Thus, the merging of small eddies into the large eddy is ~80% efficient. This is an approximate value due to variability in both the amount of PV seen in the small eddies prior to coalescence and the length of time it takes small eddies to coalesce – the eddies that coalesce first do so relatively quickly, within 18 hours of being generated (see the eddy in the black box of Figure 3.3 for an example an eddy which is third to enter the coalescence region); the last few eddies may take more than 36 hours to join up. This difference is due to the large dipole beginning to move away from the cape.

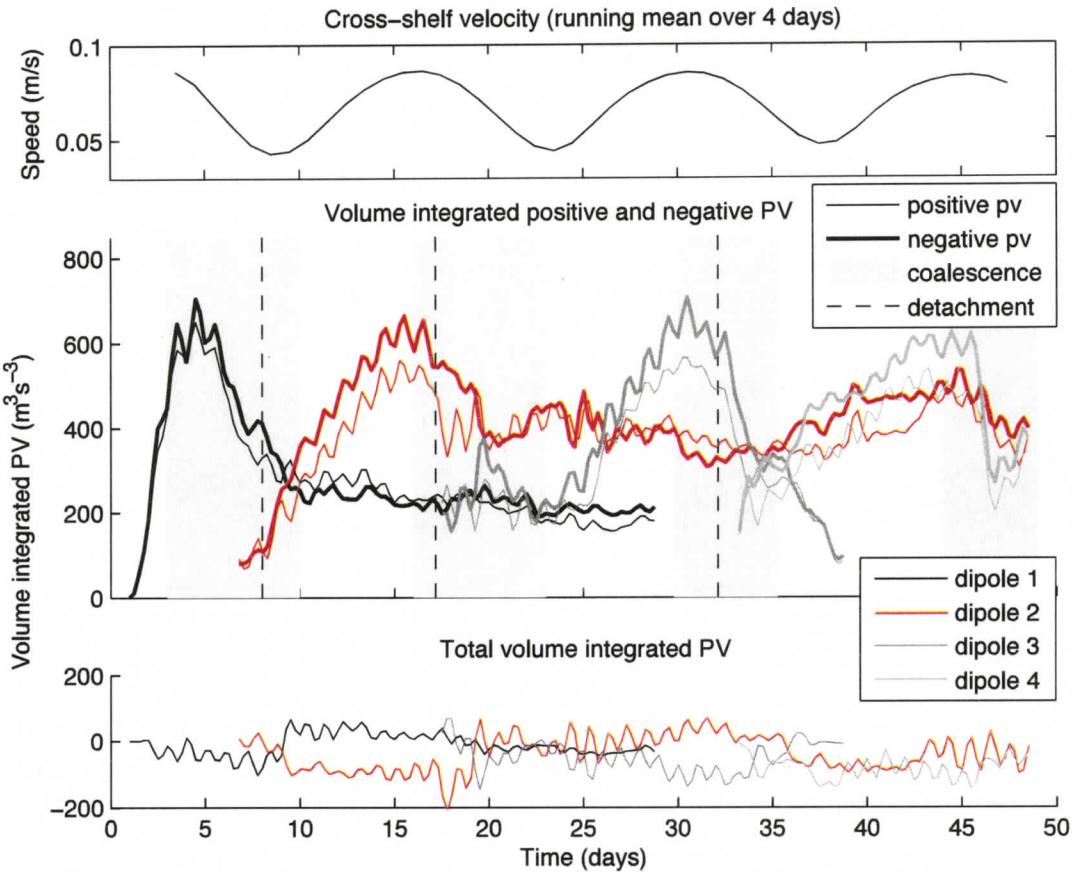

Figure 4.6 The middle frame shows volume integrated PV for each of the positive and negative PV eddies in the large dipoles. The horizontal volumes over which this integration is accomplished are shown in Figure 3.8; the integration is performed vertically between the surface and ρ=26 kgm-3. The second dipole is highlighted for further study within the text. A running mean of cross-shelf velocity is shown to illustrate the correlation between the time coalescence occurs and the time between spring and neap tide; this correlation was first noted in chapter 3. Both the middle and lower panes show that the amount of PV contained in each eddy of the dipole is approximately equal. The dashed line indicates when the dipole has detached from the cape; this measure is highly imprecise, having simply been obtained by eye; error is likely ± one day.

4.3 Asymmetry of eddy-shedding

The asymmetry of dipoles shedding to the west of the cape and never to the east is due to a tidally-rectified mean current which travels southwest across the cape tip (Figure 4.7). Crawford et al. (1995) also noted a consistent 20 cm/s flow near the tip of the cape and also concluded it was due to tidal rectification. The cyclonic (negative PV) eddy is seen in this figure, in the velocity signal to the west of the cape. A northward current is also seen running along the shelf break, as seen in other tidally-driven models for this region (Cummins and Oey, 1997).

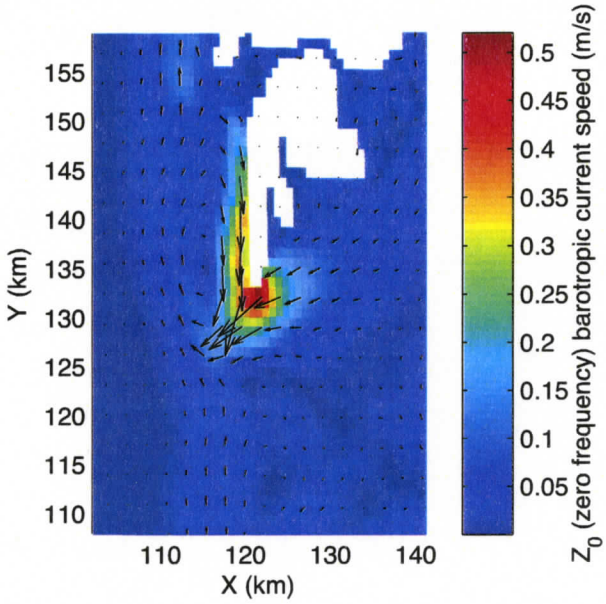

Figure 4.7 The tidal residual current at Cape St James shows a strong southwestward flow across the cape. This image was generated using the t_tide toolbox written by Pawlowicz et al., 2002.

5. Summary and Discussion

We have presented a possible method for the generation of mesoscale eddy dipoles seen sporadically near Cape St James. As the tide oscillates across the cape, small eddies rotating in alternating directions are generated by bottom friction. Between spring and neap tides many of these eddies coalesce, generating a large dipole similar to those seen in Figure 1.4. While there is no data available to validate our model eddies to show conclusively whether this mechanism is in fact responsible for their generation, the results are still of interest since we have shown a mechanism for generating mesoscale eddies via the coalescence of small headland eddies. Even if we did have data, it likely would not be particularly illuminating to validate our results since we have forced our model with tides only. If these dipoles are generated as we have shown here, they will still be affected by local winds as well as the buoyancy current seen running down the east side of the cape by di Lorenzo et al. (2005).

5.1 Reconciling headland eddy characteristics with flow parameters

5.1.1 Eddy size

The lateral size of the eddies in the final dipole corresponds well to the first baroclinic Rossby radius (~20 km over the continental shelf at this latitude, Chelton et al., 1997). However, some ingenuity is required to find what sets the size of the small eddies generated at the cape. Cenedese and Whitehead (2000) assume the final radius of an eddy generated due to buoyant outflow around a cape will be the Rossby radius; the final depth will be the depth of the generating current. They then calculate the time it would take for a continuous current to fill up this volume by assuming that all of the water in the current will go into forming the eddy. We already know that eddy formation takes 6 hours since that is the time of a single tidal ebb or flood, but we can use the same assumptions to find what the size of an eddy will be at the end of that 6 hours. The only uncertainty here is what to use for the width of the current. We can approximate this by considering the map of bottom friction shown in Figure 4.2. If we draw a line at X=122 km (ie through the tip of the cape), then we can see that the torque is large between the

cape and 9 km south of the cape. Now, we consider all of the water which flows through X=122 km between these two points as flowing into the eddy. The flow rate through this line is:

$$Q = \int_{z=0}^{surface} \int_{y=124km}^{133km} uhdydz$$

where u and h are the tidal velocity and the total water depth respectively. The total volume of the final eddy will then be:

$$V = \int_{t\ hrs}^{t+6\ hrs} Qdt.$$

For comparison to results, we have simplified this to two dimensions, vertically averaging the equation for Q; this is consistent with the assumption that the final eddy depth is the same as the depth of the generating current. So, instead of a final volume, we end up with a final surface area from which we can easily calculate a radius. These radii are shown in Figure 5.2 for each of the positive and negative eddies. The final positive PV eddies in the model have a radius of approximately 3 km; the theoretical values we have calculated here are slightly higher than that, indicating that not all of the water flowing through the high friction region contributes to eddy formation.

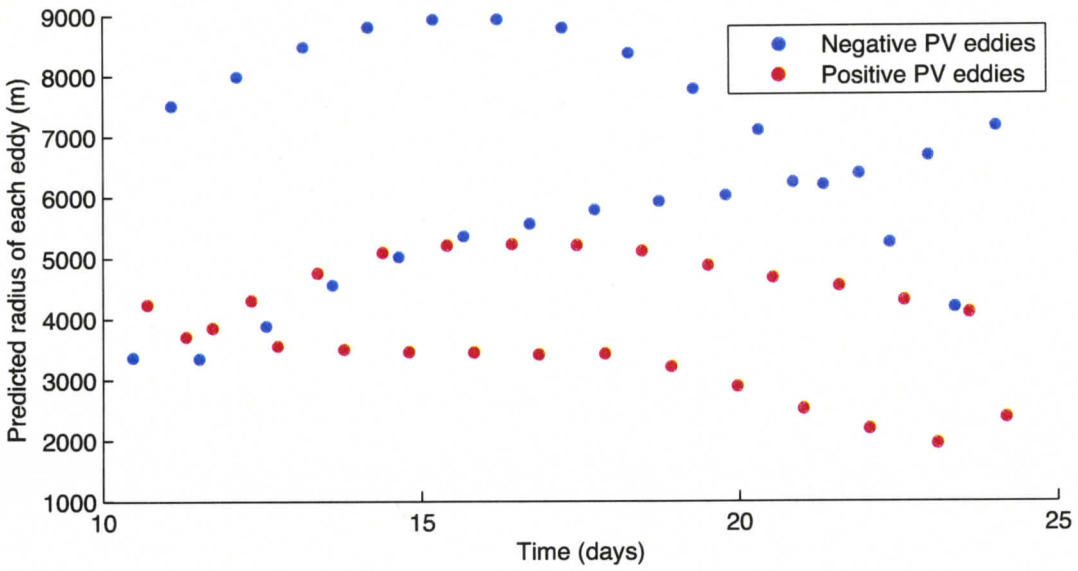

Figure 5.1 The predicted radius of each headland eddy generated between the second and third neap tides based on the volume of water flowing through the generation region shown in Figure 4.2. The radius of each of the positive PV eddies seen in the model was approximately 3 km.

5.1.2 Shedding frequency

If we consider this system as having a constant current flowing past the cape, rather than one which varies in both intensity and direction over time, then we find that the natural eddy-shedding frequency for this system is approximately 0.78 days. This is calculated using the Strouhal number for flow around a cylinder (Kundu, 2004):

$$S \equiv \frac{nd}{U_\infty}.$$

Here n is the eddy shedding frequency, d the width of the obstacle and U_∞ the flow velocity away from the obstacle. Since we have a cape rather than an island, our obstacle is essentially infinite in size, but we can approximate a value based on the width of the flow that comes in contact with the cape (~4 km). For U_∞, we use a value of 0.2 m/s which is the approximate flood or ebb speed south of the cape midway between spring

and neap tides. The value of the Strouhal number, *S*, is approximately constant at 0.21, but varies slightly with Reynolds number. The Reynolds number is (Kundu, 2004):

$$\mathrm{Re} = \frac{U_\infty d}{\nu}$$

where $\nu = 5\ m^2/s$ is the kinematic viscosity, set within the model. For the values of U_∞ and *d* defined above, we have *Re*=160 which is within the eddy shedding regime (Kundu, 2004) and gives a value of ~0.18 for the Strouhal number (Braza et. al., 1986). We can now calculate the eddy shedding frequency as *n*=9e-6 cycles/s or 0.78 cycles/day. Since we are actually generating 4 eddies/day (2 each on the ebb and flood), this means that the reversal in the tide is ripping the eddies off the cape before they've grown quite as large as they otherwise would.

5.1.3 Eddy-pairing

Whether or not a pair of counter-rotating eddies formed from oscillating tidal motion will combine to form a dipole depends on the values of two parameters: the Keulegan-Carpenter number: $K_c = U_0/\sigma a$ and the frictional Reynolds number: $R_{ef} = H/C_d\, a$. Here, $U_0 = 0.2\ m/s$ is the amplitude of the oscillating velocity, $\sigma \cong 2\ cycles/day$ is the tidal frequency, *a=2 km* is the headland width (alongshore extent), *H=100 m* is the water depth and $C_d \cong 0.001$ is the drag coefficient. These parameters describe the relative importance of advection relative to local acceleration, and advection relative to bottom friction, respectively. These values give $K_c = 4.3$ and $R_{ef} = 8.3$. Signell and Geyer (1991) suggest that values of $K_c \cong 2$ and $R_{ef} \cong 40$ are appropriate for eddy pairing and that lower values of R_{ef} will cause an eddy generated on a flood (ebb) tide to spin down before it has time to interact with the eddy generated on the following ebb (flood) tide. However, the eddies in this study tended to drift away from the cape into deeper waters when the tide reversed, causing an increase in R_{ef} and allowing the eddy to last longer than it would if it stayed closer to the cape.

5.2 Influence of tidal phasing on eddy coalescence

We have seen that positive PV eddies are only able to exit this strong current when the ebb following the generating flood is small. This implies that diurnal inequality of the tides is necessary for coalescence. To test this theory, the model was run with only the M2 tide as forcing, rather than the four constituents used in the baseline run. For the M2 only run, there was no coalescence at the cape; all eddies generated were advected northwestward immediately after generation. However, the dipole mentioned briefly in chapter 3 as forming ~50 km north of Cape St James up the west side of the Queen Charlotte Islands still appears in this model run (Figure 5.1), indicating it is more robust than the feature we discuss here. Investigation of this feature is left for future work.

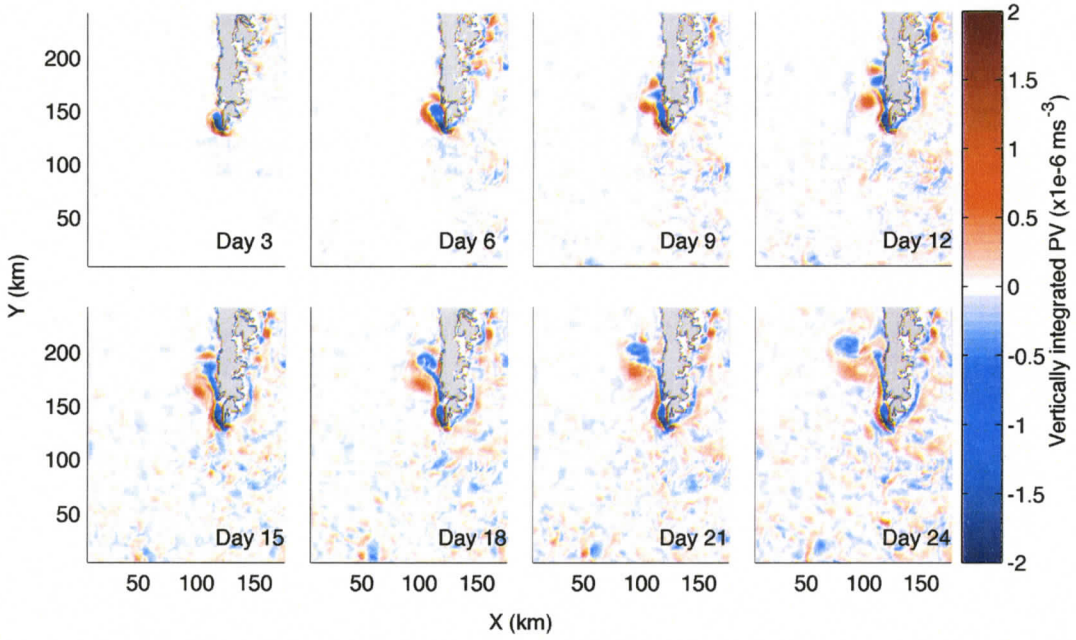

Figure 5.2 Evolution of potential vorticity integrated between ρ1=0 kgm-3 and ρ2=26 kgm-3 from day 1 to day 24 in the model run forced with M2 tides only. This figure can be compared directly to the first eight panels in Figure 3.8. Here, no dipole forms at the cape, however the feature further up the west coast of the islands is still formed. This feature is left for further investigation at another time.

As noted in chapter 3, our results depend in part on the phasing of the spring neap cycle. Coalescence of positive PV eddies only occurs for a strong generating flood followed by a weak ebb. In the model, this tidal ordering occurred between spring and neap tides. However, if the model were to run longer than the 48 days done here, we would see this ordering at different points in the cycle.

5.3 Advection of eddy dipole

The large dipole propagates under its own steam, with each eddy acting to propel the other at a speed of $\Gamma/4\pi d$, where $2d$ is the distance between the centres of the two eddies (Acheson, 1990). If we look again at the first large dipole generated, each eddy has a radius of ~8 km; and $\Gamma = \int_S \left(\frac{\partial v}{\partial x} - \frac{\partial u}{\partial y} \right) dxdy = -1.2e4 m^2/s$ in the negative eddy at 50 m depth on day 15, giving us a propagation speed of 0.12 m/s or approximately 10 km/day. The disparity between this value and the one seen in the model (6 km/day) may be attributed to wave drag due to internal waves radiating from the dipole and slowing it down (Afanassiev, 2003). More study is needed to investigate this theory.

The dipoles generated are of practical interest only if they last long enough to transport whatever nutrients or other tracers they may contain over long distances. If we consider Figure 4.6, we can estimate the decay rate of the first dipole as being about 10% between days 10 and 20. Assuming an exponential decay, this means the PV in the dipole will decay to 10% of its original value in 219 days. As stated in chapter 3, this dipole travels at a speed of ~6 km/day, so in 219 days the dipole will have traveled 1314 km. If it stays on the shelf break, this would put it off the coast of San Francisco. This is a highly approximate calculation given how little space we see the dipole for and the fact that none of the 3 dipoles generated follows exactly the same progression. We have used only the first dipole generated to get the decay scale because the second and third dipoles join together. Before this join however, the second dipole decays at a rate similar to the first.

5.4 Comparison to other eddies formed near Cape St James

5.4.1 Haida eddies

The formation and maintenance of the eddies presented here are unique in a number of ways. The most obvious comparisons to be made would be with the Haida eddy, a well-documented feature that is also formed at Cape St James. Regardless of the formation location, there are significant differences between the eddies discussed here and Haida eddies. These are:

1. Generation method: As noted in the introduction, Haida eddies are generated by the merging of mesoscale eddies generated at the cape. These mesoscale eddies are formed when a buoyancy current running southward down the east side of Cape St James separates from the coastline at the cape (di Lorenzo et al., 2005); this process is discussed in detail in the laboratory studies of Cenedese and Whitehead (2002). The eddies we have discussed here are generated by the coalescence of small headland eddies seen by Signell and Geyer (1991).
2. Scale: Haida eddies are much larger: horizontally, they have diameters up to 300 km and isopycnal depression is seen down to 1000 m depth. This vastly exceeds the scale we see here (~40 km in the horizontal, 100 m in the vertical).
3. Rotation: Haida eddies are always anticyclonic, where we are generating eddies of alternating rotation which pair to form a dipole.
4. Advection method: Haida eddies generally drift northwestward (di Lorenzo et. al., 2005) due to a combination of the planetary β effect inducing a westward drift (Gill, 1982), and a northward drift due to the topography (as in a topographic Rossby wave; described in Baines, 1995). The dipoles seen here self-advect as described above but, somewhat surprisingly, move south-southwest. This is perhaps due to the initial push given by flow at Cape St James.

5.4.2 Eddies seen by Thomson and Wilson

Similar to what we have shown here, Thomson and Wilson (1987) generated counter-rotating headland eddies through the oscillating action of the tides at Cape St. James. The model used highly idealized bathymetry, which was symmetric across the cape and

bottomed out at 100 m depth. This maximum depth allowed for a much larger region of torque-generating PV than was seen in the work presented here (where the bathymetry descends past 100 m only 5 km away from the cape), resulting in larger eddies (radii of ~10 km compared to the ~3 km eddies seen here), however the generating mechanism was the same. The eddies also did not detach from the cape, possibly due to the symmetric nature of the cape or again due to the increased torque from having a relatively shallow maximum depth.

Bibliography

Acheson, D. J. (1990). Elementary Fluid Dynamics, Oxford University Press Inc., New York, 397 p.

Afanassiev, Y (2004). Spontaneous emission of gravity waves by interacting vortex dipoles in a stratified fluid: laboratory experiments. Geophysical and Astrophysical Fluid Dynamics, 97(2), 79-95.

Arakawa, A. and V. R. Lamb (1977). Computational design of the basic dynamical processes of the UCLA general circulation model. Methods in Computational Physics, 17, 173-265.

Arango, H. G. (2004; accessed Oct. 2009). Ocean modeling discussion forum: stretching parameters – vertical coordinates (Internet). Available from https://www.myroms.org/forum/viewtopic.php?f=14&t=76&start=0

Baines, P. G. (1995). Topographic Effects in Stratified Flows. Cambridge University Press, New York, 482 p.

Ballantyne, V. A., M. G. G. Foreman, W. R. Crawford and R. Jacques (1996). Three-dimensional model simulations for the north coast of British Columbia. Continental Shelf Research, 16, 1655-1682.

Braza, M., P. Chassaing and H. Ha Minh (1986). Numerical study and physical analysis of the pressure and velocity fields in the near wake of a circular cylinder. Journal of Fluid Mechanics, 165, 79-130.

Capet, X., J. C. McWilliams, M. J. Molemaker and A. F. Shchepetkin (2008). Mesoscale to submesoscale transition in the California current system. Part 1: flow structure, eddy flux and observational tests. Journal of Physical Oceanography, 38, 29-43.

Cenedese, C. and J. A. Whitehead (2000). Eddy shedding from a cape over a sloping bottom. Journal of Physical Oceanography, 30, 1514-1531.

Chelton, D. B., R. A. deSzoeke, M. G. Schlax, K. El Naggar and N. Siwertz (1998). geographical variability of the first baroclinic rossby radius of deformation. Journal of Physical Oceanography. 28, 433-460.

Cherniawsky, J. Y., M. G. G. Foreman, W. R. Crawford, and R. F. Henry (2001). Ocean tides from TOPEX/Poseidon sea level data. Journal of Atmospheric and Oceanic Technology, 18(4), 649-664.

Choi, B. and J. L. Wilkin (2007). The effect of wind on the dispersal of the Hudson River plume. Journal of Physical Oceanography, 37, 1878-1897.

Crawford, W. R., M. J. Woodward, M. G. G. Foreman, R. E. Thomson (1995). Oceanographic features of Queen Charlotte Sound and Hecate Strait in summer. Atmosphere-Ocean, 33(4), 639-681.

Crawford, W. R., J. Y. Cherniawsky, M. G. G. Foreman and J. F. R. Gower (2002), Formation of the Haida-1998 oceanic eddy. Journal of Geophysical Research, 107(C7), 3069, doi:10.1029/2001JC000876.

Cummins, P. F. and L. Oey (1997). Simulation of barotropic and baroclinic tides off Northern British Columbia. Journal of Physical Oceanography, 27(5), 762-781.

D'Asaro, E. A. (1988). Generation of submesoscale vortices: a new mechanism. Journal of Geophysical Research, 93(C6), 6685-6693.

Di Lorenzo, E., M. G. G. Foreman and W. R. Crawford (2005). Modeling the generation of Haida eddies. Deep Sea Research, Part II, 52, 853-873.

Foreman, M. G. G., W. Callendar, A. MacFadyen, B. M. Hickey, R. E. Thomson, and E. Di Lorenzo (2008). Modeling the generation of the Juan de Fuca Eddy. Journal of Geophysical Research, 113, C03006, doi:10.1029/2006JC004082.

Foreman, M. G. G., W. R. Crawford, J. Y. Cherniawsky, R. F. Henry, and M. F. Tarbotton (2000). A high-resolution assimilating tidal model for the northeast Pacific Ocean. Journal of Geophysical Research, 105(28), 629-651.

Garrett, C (1995). Flow separation in the ocean. Proceedings of the Eighth 'Aha Huliko'a Hawaiian Winter Workshop, 119-124.

Gill, A. E. (1982). Atmosphere-Ocean Dynamics, Academic Press Inc., San Diego, 662 p.

Haney, R. L. (1991). On the pressure gradient force over steep topography in sigma coordinate ocean models. Journal of Physical Oceanography, 21(4), 610-619.

Kantha, L. H. and C. A. Clayson (1994). An improved mixed layer model for geophysical applications. Journal of Geophysical Research, 99, 25235-25266.

Kundu, P. K. and I. M. Cohen (2004). Fluid Mechanics, Academic Press Inc., San Diego, 759 p.

Marshall, J. C. and J. G. Nurser (1992). Fluid dynamics of oceanic thermocline ventilation. Journal of Physical Oceanography. 22, 583-595.

McWilliams, J. C. (1985). Submesoscale, coherent vortices in the ocean. Reviews of Geophysics, 23(2), 165-182.

Melsom, A. S., D. Meyers, J. J. O'Brien, H.E. Hurlburt and E. J. Metzger (1999). ENSO Effects on Gulf of Alaska Eddies. Earth Interactions, 3, 1-30.

Pawlak, G. and P. MacCready (2002). Oscillatory flow across an irregular boundary. Journal of Geophysical Research, 107, C5, 3036, doi: 10.1029/2000JC000596.

Pawlowicz, R., B. Beardsley, and S. Lentz (2002). Classical tidal harmonic analysis including error estimates in MATLAB using T_TIDE. Computers and Geosciences, 28, 929-937.

Serra, N., I. Ambar and R. H. Kase (2005). Observations and numerical modeling of the Mediterranean outflow splitting and eddy generation. Deep-Sea Research II, 52, 383-408.

Shchepetkin, A. F. (2007; accessed Oct. 2009). Ocean modeling discussion forum: reasonable value for maximum Haney number? (Internet). Available from: https://www.myroms.org/forum/viewtopic.php?f=14&t=612&start=0

Shchepetkin, A. F., and J. C. McWilliams (2005). The regional ocean modeling system (ROMS): a split-explicit, free-surface, topography-following coordinates ocean model. Ocean Modeling, 9(4), 347-404.

Shchepetkin, A. F., and J. C. McWilliams (2003). A method of computing horizontal pressure-gradient force in an oceanic model with a non-aligned vertical coordinate. Journal of Geophysical Research, 108(C3), 1-34.

Signell, R. P. and W. R. Geyer (1991). Transient eddy formation around headlands. Journal of Geophysical Research, 96(C2), 2561-2575.

Song, Y. T., and D. B. Haidvogel (1994). A semi-implicit ocean circulation model using a generalized topography-following coordinate system. Journal of Computational Physics, 115, 228-244.

Thomas, L. (2008). Formation of intrathermocline eddies at ocean fronts by wind-driven destruction of potential vorticity. Dynamics of Atmospheres and Oceans, 45, 252-273.

Thomson, R. E. and J. F. R. Gower (1998). A basin scale oceanic instability event in the Gulf of Alaska. Journal of Geophysical Research, 103(C2), 3033-3040.

Thomson, R. E. and R. E. Wilson (1987). Coastal countercurrent and mesoscale eddy formation by tidal rectification near an oceanic cape. Journal of Physical Oceanography, 17(11), 2096-2126.

Warner, J. C., C. R. Sherwood, H. G. Arango, and R. P. Signell (2005). Performance of four turbulence closure methods implemented using a generic length scale method. Ocean Modeling, 8, 81-113.

Warner, J. C., W. R. Geyer, and J. A. Lerczak (2005a). Numerical modeling of an estuary: A comprehensive skill assessment. Journal of Geophysical Research, 110, C05001, doi:10.1029/2004JC002691.

Whitney, F. and M. Robert (2002). Structure of Haida eddies and their transport of nutrient from coastal margins into the NE Pacific Ocean. Journal of Oceanography, 58, 715-723.